Biomaterials 303 (2023) 122394

Contents lists available at ScienceDirect

Biomaterials

journal homepage: www.elsevier.com/locate/biomaterials

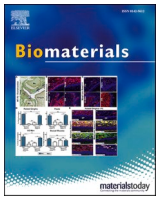

Efficient SARS-CoV-2 infection antagonization by rhACE2 ectodomain multimerized onto the Avidin-Nucleic-Acid-NanoASsembly

Simone Bernardotto [a,1], Ilaria Frasson [b,1], Silvia Faravelli [c], Annalisa Morelli [d,g], Elisa Schiavon [a], Giulia Yuri Moscatiello [d], Martina Bruna Violatto [d], Alberta Pinnola [c], Anselmo Canciani [c], Andrea Mattarei [a], Gianpaolo Rossi [e], Marisa Brini [f], Laura Pasetto [h], Valentina Bonetto [h], Paolo Bigini [d], Federico Forneris [c], Sara N. Richter [b,i,**], Margherita Morpurgo [a,*]

[a] Pharmaceutical and Pharmacological Sciences Dept (DSF), University of Padova, Via Marzolo, 5. 35131, Padova, Italy
[b] Department of Molecular Medicine (DMM), University of Padova, Via A. Gabelli, 63, 35121, Padova, Italy
[c] The Armenise-Harvard Laboratory of Structural Biology, Dept. Biology and Biotechnology, University of Pavia, Via Ferrata 9/A, 27100, Pavia, Italy
[d] Department of Biochemistry and Molecular Pharmacology, Istituto di Ricerche Farmacologiche Mario Negri IRCCS, Italy, Via Mario Negri 2, 20156, Milano, Italy
[e] Department of Medicine (DIMED), University of Padova, Via Giustiniani, 2, 35131, Padova, Italy
[f] Department of Biology (DIBIO), Viale G. Colombo, 3, 35131, Padova, Italy
[g] Department of Biotechnology and Biosciences, University of Milano-Bicocca, Piazza della Scienza 2, 20126, Milano, Italy
[h] Department of Neuroscience, Istituto di Ricerche Farmacologiche Mario Negri IRCCS, Italy, Via Mario Negri 2, 20156, Milano, Italy
[i] Microbiology and Virology Unit, Padua University Hospital, 35121, Padua, Italy

ARTICLE INFO

Keywords:
Viral prevention
Viral decoy
SARS-CoV-2
Functional nanoparticles
Avidin-biotin
Avidin-nucleic-acid-NanoASsembly

ABSTRACT

Nanodecoy systems based on analogues of viral cellular receptors assembled onto fluid lipid-based membranes of nano/extravescicles are potential new tools to complement classic therapeutic or preventive antiviral approaches. The need for lipid-based membranes for transmembrane receptor anchorage may pose technical challenges along industrial translation, calling for alternative geometries for receptor multimerization. Here we developed a semisynthetic self-assembling SARS-CoV-2 nanodecoy by multimerizing the biotin labelled virus cell receptor -ACE2- ectodomain onto a poly-avidin nanoparticle (NP) based on the Avidin-Nucleic-Acid-NanoASsembly-ANANAS. The ability of the assembly to prevent SARS-CoV-2 infection in human lung cells and the affinity of the ACE2:viral receptor-binding domain (RBD) interaction were measured at different ACE2:NP ratios. At ACE2:NP = 30, 90 % SARS-CoV-2 infection inhibition at ACE2 nanomolar concentration was registered on both Wuhan and Omicron variants, with ten-fold higher potency than the monomeric protein. Lower and higher ACE2 densities were less efficient suggesting that functional recognition between multi-ligand NPs and multi-receptor virus surfaces requires optimal geometrical relationships. In vivo studies in mice showed that the biodistribution and safety profiles of the nanodecoy are potentially suitable for preventing viral infection upon nasal instillation. Viral receptor multimerization using ANANAS is a convenient process which, in principle, could be rapidly adapted to counteract also other viral infections.

1. Introduction

In the context of the fight against viral infections, "decoy" systems based on the use of analogues of viral cellular receptors [1,2] as single molecules or assembled onto fluid lipid-based membrane nanoparticles represent new tools potentially capable of complementing classic therapeutic or preventive approaches based on antibodies, hyperimmune sera and vaccines. Decoy systems are designed to act as “baits” for the virus capable of diverting it from its target cells and blocking it before it infects them. Compared to the preventive/treatment options currently available in the clinic, major advantage of these systems stems from the fact that their efficacy is not affected by viral mutations.

* Corresponding author. Pharmaceutical and Pharmacological Sciences Dept (DSF), University of Padova, Via Marzolo, 5. 35131, Padova, Italy.
** Corresponding author. Department of Molecular Medicine (DMM), University of Padova, Via A. Gabelli, 63, 35121, Padova, Italy.
E-mail addresses: sara.richter@unipd.it (S.N. Richter), margherita.morpurgo@unipd.it (M. Morpurgo).
[1] Equal contribution.

https://doi.org/10.1016/j.biomaterials.2023.122394
Received 30 June 2023; Received in revised form 18 October 2023; Accepted 9 November 2023
Available online 16 November 2023

During the recent COVID-19 pandemic, the decoy concept, whose efficacy has been initially demonstrated against the influenza virus [2] and HIV [1] has also been suggested to develop new tools against SARS CoV-2.

SARS-CoV-2 infection is triggered by the binding of its envelope - Spike (S)- protein to the cell target membrane angiotensin-converting enzyme 2 (ACE2) [3,4]. S Protein–ACE2 binding allows viral attachment to cells, which is followed by viral S-protein priming by the TMRSS2 protease, membrane fusion, and viral entry [3]. The interaction with ACE2 is also responsible for increased angiotensin II levels and activation of the renin-angiotensin system, which further increases ACE2 expression [5] and plays a critical role in the severe acute lung injury induced by SARS-CoV viruses.

Decoy strategies against SARS-CoV-2 infection tackle the S-protein/ACE2 interaction using ACE2 analogues as baits for the virus. It was shown that a recombinant soluble version of the ACE2 receptor (rh-*s*-ACE2) is capable to inhibit SARS-CoV-2 infection in a concentration dependent manner [6], both *in vitro* and in clinical studies in a small number of patients [7]. Following these landmark results, other ACE2-based viral decoy systems have been proposed towards higher efficacy, either by inducing *in vivo* transient rh-*s*-ACE2 mucosal expression by means of mRNA lipid-based nanoparticles [8] or by engineering rh-*s*-ACE2 towards higher affinity for the S protein [9–11]. In addition, ACE2-based nanodecoy systems based on membrane-anchored ACE2 membrane vesicles have also been investigated [12–16] showing high efficacy, likely due to the synergistic effect of multiple ACE2 units present at the vesicle membrane. However, despite the great potentials demonstrated by these ACE2-carrying nano/extra vesicles, their clinical translation may be hampered by the complexity in their production standardization. Therefore, alternative synthetic or semisynthetic tools for ACE2 nano-multimerization that reproduce the synergistic effect observed with the nano/extra vesicles, may markedly accelerate the clinical translation of this therapeutic strategy.

In this context a semisynthetic convenient tool for protein multimerization is the Avidin-Nucleic-Acid-Nano-ASsembly (ANANAS) platform. ANANAS are nanosized (Ø = 120 nm) colloidally stable polyavidin toroids generated from the condensation of a non-coding nucleic acid (NA) filament by the high-affinity interaction with egg-white avidin [17,18]. ANANAS can be decorated at their surface, in one pot solution with up to 1000 functionalities (provided that these can be biotinylated) at stoichiometric control thanks to their intact biotin-binding capability and the high affinity for biotin ligands (Kd 10^{-15} M^{-1}) [19]. Decoration occurs by simply mixing with biotinylated functional elements at desired biotin:biotin binding sites (BBS) molar ratios and if neither the BBS become saturated nor the surface area available is exceeded [19,20], no purification is necessary. In principle, if these two requirements are fulfilled, an infinite number of surface composition combinations can be conveniently generated and screened so that, in principle, selection of the best performing composition is facilitated.

Successful application of this platform has been demonstrated in *in vitro* and *in vivo* diagnostics [21,22] and in drug delivery [23,24]. Thanks to the tolerogenic property of avidin [25,26], these nanocarriers show no toxicity and poor immunogenicity even after multiple administration in mice for up to 30 days [24]. When administered parenterally they circulate freely in the bloodstream for more than 6 h and are later captured by scavenging organs such as liver and spleen, from which they are degraded within 48 h. An additional property that makes them suitable for pharmaceutical development is their highly defined composition which makes them suitable for scaling up studies.

In this work ANANAS were used as scaffold to generate multimerized ACE2 ectodomain to improve the avidity for the SARS-CoV-2 S protein with the ultimate goal of preventing SARS-CoV-2 cell invasion. To this end, a monomeric biotin derivative of ACE2 ectodomain was optimized by recombinant DNA technologies. ACE2:NP assemblies were generated at different ACE2-biotin:NP molar ratios and compared for size and affinity for the viral S protein RBD of both the Wuhan and the new variant of concern Omicron (BA.1) which emerged later on and became dominant worldwide [27,28]. The ability to prevent SARS-Cov-2 infection of the two variants in human lung cells was also tested as a function of ACE2 density at nanoparticle surface and compared to that of the monomeric rh-sACE2-biotin. *In vivo* preliminary biodistribution and toxicity studies in healthy mice were then performed to assess the possibility of nasal administration.

2. Materials and methods

ANANAS core nanoparticles were obtained in freeze dried form as described elsewhere using avidin from e.protein (Belgium) and biotin-PEG5kDa (Laysan Bio) for colloidal protection [17]; Biotin-diaminohexanamido-Alexa633 (biotin-C6-Alexa633) was obtained in the lab according to published procedures [22]; biotin-HRP (code BH-0101) and ELISA Dilution buffer (DB) were from ANANAS nanotech (Padova, Italy). SARS-CoV-2 (COVID-19) Spike receptor-binding domain (RBD) Wuhan-Hi-1 variant was produced recombinantly as described in Ref. [29]; RBD B.1.1.7/Alpha (English), and B.1.617.1/Kappa (Indian) variants were purchased from Genetex (Irvine, California, USA).

Cell culture and virus- Vero E6 (ATCC® CRL-1586™) were maintained in Dulbecco's modified Eagle's medium (DMEM; Thermo Fisher Scientific), Calu-3 cells (ATCC®, HTB-55) were maintained in Dulbecco's Modified Eagle Medium: Nutrient Mixture F-12 (DMEM/F-12, Thermo Fisher Scientific). Media were supplemented with 10 % (v/v) fetal bovine serum (FBS, Thermo Fisher Scientific) and penicillin/streptomicin (Thermo Fisher Scientific). Cell cultures were maintained at 37 °C and 5 % CO_2 in humidified atmosphere and routinely tested for mycoplasma contamination. For seeding and subcultivation, cells were first washed with phosphate buffered saline (PBS) and then incubated in the presence of trypsin/EDTA solution (Gibco, Thermo Fisher Scientific) until cells detached.

The SARS-CoV-2 Wuhan isolate SARS-CoV-2/human/ITA/CLIMVIB2/2020 was provided by the Virology Unit of Ospedale Luigi Sacco (GenBank accession ON062195 MW000351.1)(Milan, Italy). The SARS-CoV-2 Omicron variant was provided by the Microbiology Unit of the University-Hospital of Padova (Padova, Italy), and previously described (GenBank accession ON062195). All viral stocks were prepared by propagation in Vero E6 cells in DMEM supplemented with 2 % FBS. Viral titre was assessed by plaque reduction assay (PRA) and expressed as plaque forming units (PFU) per milliliter (ml). All experiments involving live SARS-CoV-2 were performed in compliance with the Italian Ministry of Health guidelines for Biosafety Level 3 (BSL-3) containment procedures in the approved laboratories of the Molecular Medicine Department of University of Padova.

Molecular cloning – The sequence encoding for human ACE2 ectodomain (Uniprot Q9BYF1 residues 18–615) was amplified from a pCEP4-myc-ACE2 (Addgene plasmid # 141185) [30] using polymerase chain reaction with oligonucleotides *Bcl*I-ACE2-Fw (aaaatgatcaTCCACCATTGAGGAACAGGCC) and ACE2-*Not*I-Rv (aaaagcggccgcGTCTGCATATGGACTCCAGTC). The resulting sequence was processed with 5′-*Bcl*I and 3′-*Not*I restriction endonucleases for subsequent transfer into a modified pUPE.107.03-BAP (U-Protein Express BV) expression vector bearing a C-terminal 6xHis-tag followed by a Biotin Acceptor Peptide (BAP) sequence (GLNDIFEAQKIEWHE [31]). All sequences underwent checking for their correctness using Sanger sequencing (Microsynth). The plasmid used for *in vivo* biotinylation, encompassing the *E. coli* BirA sequence (UniProt P06709) followed by a KDEL sequence for retention in the endoplasmic reticulum (pUPE.107.03-BirA-KDEL) was a kind gift from U-Protein Express B.V.

Recombinant production of hACE2 ectodomain fragments - Recombinant hACE2 ectodomain *(rh-s-ACE2)* was produced using HEK293-F cells (Invitrogen) cultivated in suspension using Freestyle medium (Invitrogen) as described in Ref. [32] Briefly, cells were co-transfected at

a cell density of 1 million mL^{-1} using 1.0 μg of pUPE.107.03-BAP-hACE2and 3 μg of polyethyleneimine (PEI; Polysciences). For *in vivo* biotinylation, a DNA mixture composed of 0.2 μg of pUPE.107.03-BAP-hACE2 and 0.2 μg of pUPE.107.03-BirA-KDEL was used. All cultures were supplemented with 0.6 % Primatone RL (Merck) 4 h after transfection. The cell media containing secreted proteins were collected 6 days after transfection by centrifugation at 1000×*g* for 15 min. The pH and ionic strength of the filtered medium were adjusted using concentrated phosphate buffer saline (PBS). Samples were loaded onto a 5 mL His-Trap Excel column (Cytiva) using a peristaltic pump and then eluted with a 0–250 mM imidazole gradient using a NGC fast protein liquid chromatography (FPLC) system (Bio-Rad). Iodoacetamide treatment to generate either rh-*s*-ACE2i or *rh-s-ACE2i-biotin* was performed on the eluted samples (rh-*s*-ACE2 or rh-*s*-ACE2-biotin, respectively) through incubation with 25 mM iodoacetamide (Merck) for 1 h to block the reactivity of free cysteine residues, followed by concentration with concomitant buffer exchange with fresh PBS to remove imidazole using Amicon centrifugal filters (Merck). All samples were concentrated to 1 mg mL^{-1}, flash-frozen in liquid nitrogen and kept at −80 °C until usage.

Recombinant protein QC prior to usage - Quality control during protein purification was carried out using reducing and non-reducing SDS-PAGE analysis and differential scanning fluorimetry (DSF) with a Tycho NT.6 instrument (Nanotemper). Evaluation of effective biotinylation was assessed through western blotting using HRP-conjugated streptavidin (Merck). For detection, the membranes were incubated with Clarity ECL substrate (Bio-Rad) and imaged in a ChemidocMP imaging system (Bio-Rad). Image processing and densitometry analyses were carried out using the Image Lab software (Bio-Rad).

rh-s-ACE2i-biotin:ANANAS assemblies - Non-functionalized ANANAS "core" assemblies were obtained in freeze-dried form according to optimized procedures published elsewhere [17]. For ACE2 decoration, core nanoparticles were re-dissolved at 0.1–1 mg mL^{-1} in 10 mM phosphate, pH 7.4 + 0.0125 % tween20, and mixed with *rh-s-ACE2i-biotin* or ANANAS Diluent Buffer (DB, ANANAS nanotech S.r.l., Padova, Italy) at predetermined molar ratios. Assembly size was determined by dynamic light scattering (DLS) using a Malvern Ultrasizer apparatus. To quantify the nanoparticle loading capacity for rh-*s*-ACE2-biotin, assembly solutions generated at ACE2:NP molar ratios between 30 and 90 were analyzed by gel permeation chromatography using a fast protein liquid chromatography system (FPLC, Akta purifier, GE). Samples were eluted (1 mL/min) using PBS in a Superose 6 prep® medium (Tricorn®10/300 column) which allows to separate NP-associated rh-*s*-ACE2-biotin from the one in solution.

Affinity of rh-s-ACE2i-biotin for SARS-CoV-2 RBD - The affinity of *rh-s-ACE2i-biotin* (as free molecule or assembled onto ANANAS) for the different SARS-CoV-2 RBD variants was tested by Enzyme Linked ImmunoSorbed Assay (ELISA). Briefly, Nunc® Maxisorp 96-well plates were conditioned by overnight (4 °C) incubation with the RBD (0.2 μg/ml) in 50 mM carbonate buffer pH 9.5. After blocking for 30 min with 3 % BSA in 10 mM phosphate, 150 mM NaCl, pH 7.4 + 0.05 % tween20 (PBST), wells were incubated for 2h at room temperature (RT) with serial dilutions of *rh-s-ACE2i-biotin* from 0.625 to $3.18x10^{-5}$ μg/mL (between $9x10^{-9}$ and $3.5x10^{-11}$ M) in DB. When testing rh-*s*-ACE2-biotin as free molecule in solution, detection was carried out after incubation with avidin-HRP (Sigma-Aldrich, 1 μg/mL in DB, 45 min, RT), followed by reaction with 100 μL of tetramethylbenzidine (TMB, SureBlue Reserve, KPL immunoassays Reagents, Gaithersburg, MD USA) and blocking with 100 μL of 1 M H_2SO_4. When testing the protein assembled with ANANAS or mixed with avidin, detection was carried out after incubation with biotin-HRP (1 μg/mL in DB, 45 min, RT) followed by TMB detection as above. To determine the experimental dissociation constants (Kds), the plots of absorbance at 450 nm *versus* rh-*s*-ACE2-biotin concentration were fitted by the *Graphpad-Prism*® software using the *One site - Specific binding* algorithm.

Transmission Electron microscopy (TEM) - Solutions (in 10 mM HEPES buffer, pH 7.4) of ANANAS, ANANAS-ACE2-30, and SARS-CoV-2 (Wuhan variant) - as such, or preincubated (10' in ice) with ANANAS or ANANAS-ACE2-R30 - were fixed with 4 % PFA (in ice) for 60 min, and one drop (50 μL) was placed on a 400-mesh holey-film grid for 10 min. After washing with PBS, samples were stained with 1 % uranyl acetate for 2 min and washed with PBS. Finally, biotin functionalized gold nanoparticles (5 nm) (Thermofisher-AlphaAesar) (dilution 1:5000) in water were added for ANANAS staining. Samples were observed with a Tecnai G2 (FEI; Thermo Fisher Scientific, Waltham, MA, USA) transmission electron microscope operating at 100 kV. Images were captured with a Veleta (Olympus Soft Imaging System; Münster, Germany) digital camera. The initial viral titer in all spotted solutions was $2.8x10^6$ PFU/μl. Mixtures with ANANAS or ANANAS-ACE2-30 were generated a NP: PFU molar ratio = 100.

Antiviral assays - Calu-3 cells ($2.75x10^4$ cells/well) were seeded in 96 well plates 24 h prior to infection. The cell culture medium was removed and replaced with virus inoculum (MOI of 0.1 PFU/cell), previously incubated with *rh-s-ACE2i-biotin* in solution or assembled onto ANANAS at ACE2:NP molar ratio equal to 0 (ANANAS), 15 (ACE2:NP-R15), 30 (ACE2:NP-R30) or 60 ACE2:NP-R60, or with vehicle (DB). Following 1 h adsorption at 37 °C, the virus inoculum was removed and replaced with fresh 10 % FBS DMEM/F-12 media. Cells were incubated at 37 °C for 30 h before supernatants were harvested. The viral titer (expressed as PFU/ml) was calculated by PRA in Vero E6 cells.

SARS-CoV-2 titration by plaque reduction assay (PRA) - Vero E6 cells were seeded in 24-well plates at a concentration of 9×10^4 cells/well. The following day, serial dilutions of the viral stocks or of the tested supernatants were performed in serum-free DMEM media. After 1 h absorption at 37 °C, the overlay media was added to the inoculum to give a final concentration of 2 % (v/v) FBS/DMEM media and 0.6 % (v/v) methylcellulose (Merck Life science, Cat: M0512) to achieve a semi-solid overlay. Samples were incubated at 37 °C for 48 h, next fixed using 5 % Formaldehyde in PBS (Merck Life Science, Cat: 252549). Plaques were visualized using Crystal Violet solution (20 % Ethanol, Merck Life science, Cat: C6158).

Cytotoxicity - The cytotoxicity of the tested ANANAS nanoparticles was assessed and expressed as cytotoxic concentration (CC_{50}). Calu-3 cells ($2.75x10^4$ cells/well) were seeded in 96 well plates and the tested nanoparticles or an equal volume of vehicle (Diluent Buffer, ANANAS Nanotech S.r.l., Padova, IT) were supplemented to the medium. ANANAS nanoparticles were incubated for 48 h and cell viability was determined by measuring the adenosine triphosphate (ATP) content of the cells using the ATPlite kit (PerkinElmer, Waltham, MA, Cat: 6016941) according to the manufacturer's instructions. CC_{50} values were calculated using the Reed and Muench method [33].

Animals – The "Mario Negri" Institute for Pharmacological Research IRCCS adheres to the principles set out in the following laws, regulations, and policies governing the care and use of laboratory animals: Italian Governing Law (D.lgs 26/2014; Authorization no. 19/2008-A issued March 6, 2008 by Ministry of Health); Mario Negri Institutional Regulations and Policies providing internal authorization for persons conducting animal experiments (Quality Management System Certificate, UNI EN ISO 9001:2015, Reg. No. 6121); the NIH Guide for the Care and Use of Laboratory Animals (2011 edition), and EU directives and guidelines (EEC Council Directive 2010/63/UE). This work was reviewed by the IRCCS-IRFMN Animal Care and Use Committee (IACUC) and then approved by the Italian "Istituto Superiore di Sanità" (code: 49/2021-PR). Eight-week-old female CD1 mice were maintained under specific pathogen-free conditions in the Institute's Animal Care Facilities; they received food and water ad libitum and were regularly checked by a veterinarian who is responsible for animal welfare supervision and experimental protocol review.

Biodistribution in vivo - Mice were anesthetized with medetomidine (Domitor®) at a dose of 0,4 mg/kg b.w. and ketamine (Lobotor®) at a dose of 36 mg/kg injected intraperitoneally. Nanoformulations (ACE2: NP-R30 or core ANANAS -ANANAS) or vehicle was administered

intranasally with a micropipette (25 μl per nostril with a total volume of 50 μl). Animals were allowed to recover immediately afterwards (Antisedan® - 0,8 mg/kg). A total of 27 CD1 animals were used. Twelve mice were treated with 51,6 μg of NPs/mouse (2 mg/kg) of ANANAS and twelve mice with ACE2:NP-R30 51,6 μg of NPs/mouse (2 mg/kg) loaded with 0.2 mg/kg of ACE2 (5 μg *rh-s-ACE2i-biotin*/dose). The remaining three mice were treated with PBS and were used as controls. At the end of the study, mice were euthanized 15 min, 2, 24, and 72 h after treatment with cervical dislocation. Liver, kidney, spleen and lungs were collected and scanned for ex vivo imaging. Spectral unmixing, image processing, and analysis were done using Living Image 4.3.1 software (PerkinElmer).

Tissue Collection and Histological Analysis - For immunofluorescence analysis, at the moment of sacrifice, lungs were collected, frozen in dry ice and stored at −80 °C until immunofluorescence staining. Cryostat sections were cut at 20 μm and mounted on glass slides. Slides were postfixed in 10 % formalin (Bioptica) for 20 min, washed three times in phosphate-buffered saline (PBS) for 5 min and incubated for 1 h with a blocking solution (PBS-NGS 10%-Triton X-100 0.1 %) then washed again with PBS. For subcellular localization, the antibody anti-CD68 (specific for lysosome and endosome membranes of macrophages) was employed as follows: primary monoclonal rat antibody anti-CD68 (1:200, Serotec, Kidlington, UK) + Triton X-100 0.1 % + NGS 3 % in PBS overnight (O/N) at 4 °C. For PEG staining: primary monoclonal rabbit antibody anti-Polyethylene glycol (1:165, Abcam RabMab ab51257) + Triton X-100 0.1 % + NGS 3 % in PBS O/N at 4 °C. After washing, secondary alexa488 conjugated antibody (Invitrogen) (1:500) was incubated for 1 h at RT in a 1 % PBS-NGS solution. Then, the slides were washed and nuclei were stained with Hoechst 33258 (2 μg/mL in PBS, for 10 min). For the histological evaluation, lungs were removed from treated animals at different timepoints (15 min, 2, 24 and 72 h) and fixed overnight in 10 % formalin and were embedded in paraffin and cut into 4 μm-thick sections. Slices were deparaffinised in Xylene and rehydrated through a series of alcohols to water. Hematoxylin-Eosin (BioOptica) staining method was used to investigate lung injury. Sections were visualized through Olympus virtual slide microscope VS120 (Olympus, Japan).

Cytokine measurements - Serum levels of IL-10, INF-γ and TNF-α were measured using commercially available AlphaLISA kits (#AL502C, #AL593C, #AL541C), as described by the manufacturer (PerkinElmer). AlphaLISA signals were measured using an Ensight Multimode Plate Reader (PerkinElmer).

3. Results

3.1. Optimizing biotinilation of rh-s-ACE2 ectodomain

The preparation of semi-synthetic multi-assemblies requires the use of components with defined and reproducible properties. In particular, multi-assembly using the poly-avidin ANANAS core necessitates the use

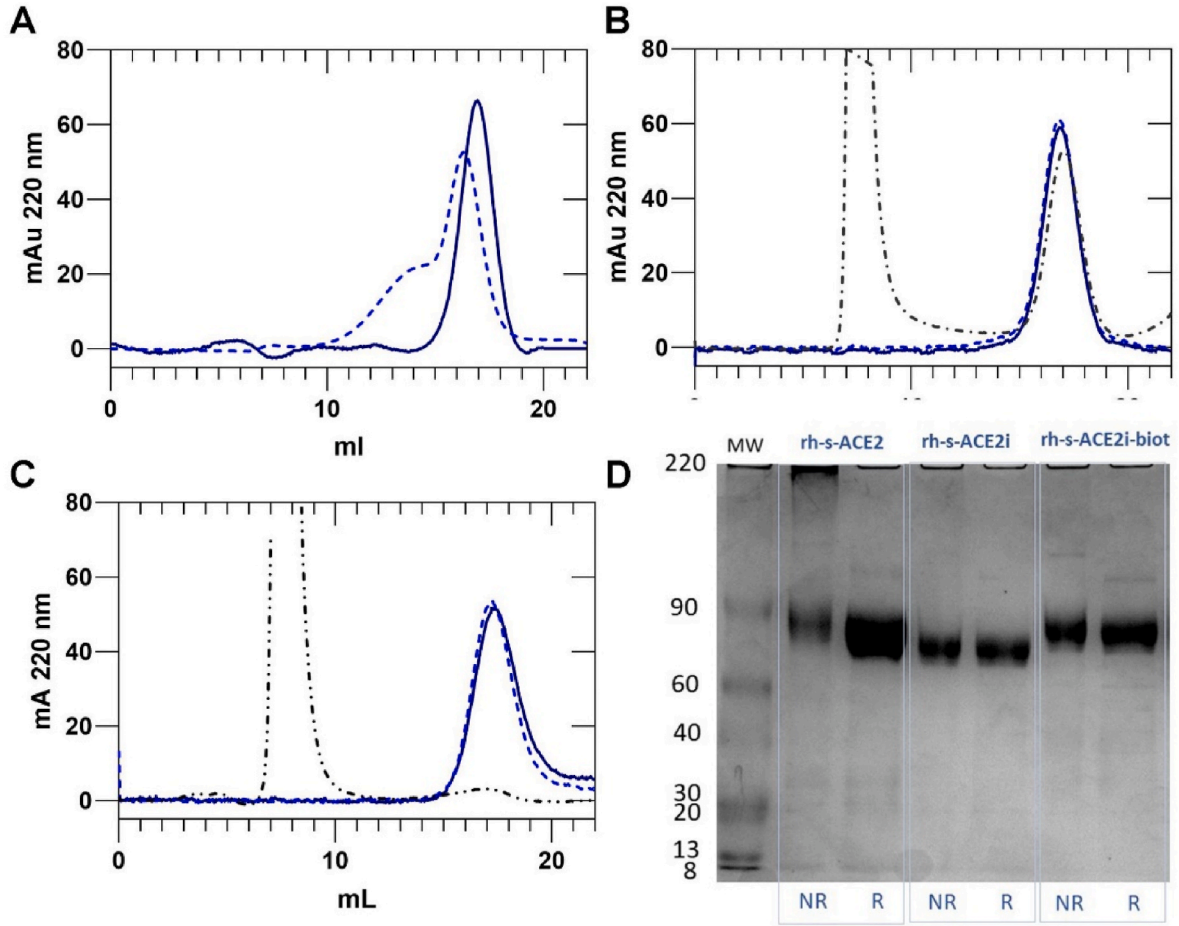

Fig. 1. Gel permeation chromatograms and SDS-Page analysis of different rh-*s*-ACE2 products. A) rh-*s*-ACE2, B) rh-*s*-ACE2i and C) *rh-s-ACE2i-biotin*, as prepared (full line) and after 24 h storage at 4 °C in PBS buffer (dashed lines). Rh-*s*-ACEi reacted with biotin-C6-NHS and *rh-s-ACE2i-biotin* were also analyzed after mixing with ANANAS (ACE2:NP = 30 mol:mole) (dash-dot lines). Only if biotinylated the protein binds to ANANAS and elutes together with the nanoparticle fraction with a retention volume of about 8 mL; D) SDS-PAGE (4–15 %) analysis of the different rh-*s*-ACE2 products after 24 h storage at 4 °C, conducted in reducing (R) and non-reducing (NR) conditions. The expected protein (MW ~ 69500 Da) displays a band at around 70 kDa. The high MW smeared signal in the NR rh-*s*-ACE2 sample corresponds to protein multimers, which are reverted to the expected monomeric protein by the reducing (R) treatment.

of biotinylated ligands. Preliminary studies (Fig. S1 in supplementary Information S.I. file) were carried out to identify the best strategy for obtaining a recombinant human soluble ACE2 (ACE2 ectodomain, rh-*s*-ACE2) biotin derivative with suitable properties for ANANAS tethering. SDS-PAGE and gel filtration chromatography analysis (Fig. 1A and D) highlighted the tendency of the recombinant ACE2 ectodomain to multimerize/aggregate secondary to SS bond formation. In fact, while freshly prepared rh-*s*-ACE2 elutes in gel permeation chromatography as a single peak at about 17 mL retention volume, a second peak at lower retention appears after 24h storage at 4 °C. SDS-PAGE electrophoresis of the same sample showed the presence of large MW aggregates, which reverted to the expected MW upon reductive treatment. *Rh-s-ACE2* not only had the tendency to aggregate but also was found difficult to biotinylate through classic bioconjugation tools. In fact, the product of reaction with 10 equivalents of a biotin-*N*-hydroxy succinimide ester derivative was not retained by the ANANAS core. A thiol-capped rh-*s*-ACE2 derivative was thus generated by S-iodoacetamide reaction of cysteines. The resulting protein (*rh-s-ACE2i*) lost the tendency to aggregate but, again, it was difficult to biotinylate by classic bioconjugation procedures, as less than 10 % of the product of biotin conjugation was retained by the nanoparticles (Fig. 1B). Finally, a S-iodacetamide-capped biotin derivative (*rh-s-ACE2i-biotin*) was obtained by inserting the biotin acceptor peptide (BAP) tag (also known as AVI tag) after the His-tag (AAAHHHHHH-MS-GLNDIFEAQKIEWHE) [34] at the protein C terminus using recombinant DNA technologies. Usage of BAP tagging for localized protein biotinylation is well established. This process typically relies on *in vitro* treatment of purified BAP-tagged proteins with soluble *E. coli* BirA enzyme, which specifically recognizes the BAP sequence attaching biotin to the free amino group found on the side chain of the lysine residue. To minimize sample handling and ensure homogeneity, we have relied on the possibility of applying the same strategy directly inside transfected cells [35], by co-transfecting HEK293-F cells with a plasmid encoding for rh-*s*-ACE2-BAP and a second plasmid containing E. coli BirA preceded by a Cystatin signal peptide and fused to a C-terminal retention signal for the endoplasmic reticulum. The resulting product was stable against aggregation and was efficiently biotinylated, as demonstrated by its ability to be completely retained by ANANAS (Fig. 1C).

3.2. *ACE2:ANANAS pre-formulation*

Pre-formulation studies were carried out to quantify the loading capability of the NPs for *rh-s-ACE2i-biotin* and to assess the colloidal stability of the multimerized system as a function of ACE2 density at the NP surface. To assess the NP capability for *rh-s-ACE2i-biotin*, the protein was mixed with ANANAS at molar ratios varying between 15 and 120. Mixtures were analyzed by dynamic light scattering (DLS) and gel permeation chromatography to evaluate the size of the assemblies and the amount of NP-bound/unbound rh-*s*-ACE2-biotin, respectively. In addition, ζ-potential measurements were carried to measure the effect

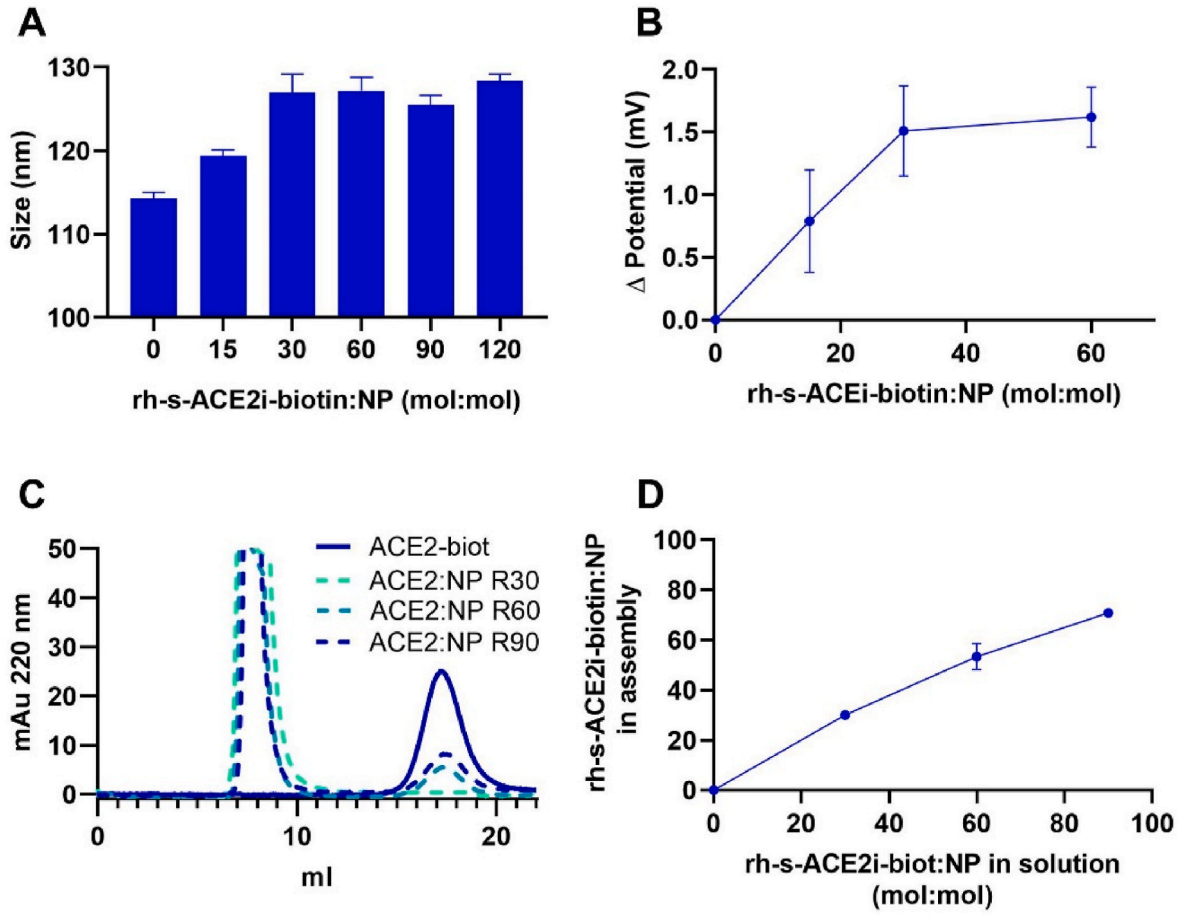

Fig. 2. Pre-formulation studies. A) Size of *rh-s-ACE2i-biotin*:ANANAS assemblies at ACE2:NP molar ratio in solution between 15 and 120; B) Assemblies Z-potential as a function of *rh-s-ACE2i-biotin*:NP molar ratio in solution mixture. Values were measured in PBS buffer, where core ANANAS exhibit a slightly negative value of −15.43 mV; **C)** Gel permeation chromatograms of *rh-s-ACE2i-biotin* (5 μg/run) as such or when mixed with ANANAS at molar ratios ACE2:NP equal to 30, 60 and 90. The peak at retention volume of about 17 mL corresponds to the free protein, the peak at 8 mL corresponds to the nanoassembly; **D)** Number of *rh-s-ACE2i-biotin* molecules linked onto the NPs as a function of the ratio of ACE2i-biotin:NP in solution mixtures. Values were calculated from the chromatograms of panel C by comparing the areas of the *rh-s-ACE2i-biotin* peak in the assembly mixtures with that of the protein in the absence of the nanoparticles.

of ACE2 loading onto the NP surface charge. Core nanoparticles displayed a size of about 114 nm and a rise in size up to about a maximum of 128 nm was observed by increasing the ACE2:NP in solution (Fig. 2A). This increment is compatible with the build-up of a ~7 nm monolayer of rh-*s*-ACE2 around core nanoparticles, in line with the protein dimensions registered by X-ray crystallography [36]. NP size increase was proportional to the amount of *rh-s-ACE2i-biotin* in solution up to ACE2:NP ratio = 30; no further size increment was registered at higher molar ratios. On the other hand, ζ-potential measurements and gel permeation chromatography (Fig. 2B) collectively indicate that the NP capacity for *rh-s-ACE2i-biotin* is greater than 30. In fact, while NPs display (in PBS) a neutral to slightly negative surface charge (−15.43 mV), the ζ-potential becomes systematically less negative as the ACE2:NP ratio increases, reaching a plateau at 60 ACE2:NP. In line with these data, gel permeation chromatograms of mixtures obtained at increasing ACE2:NP ratio reveal that the number of *rh-s-ACE2i-biotin* units bound/NP is 30, 53 and 71 at ACE2:NP ratios in solution of 30, 60, or 90, respectively (Fig. 2C and D). Overall, these data demonstrate that a maximum nanoparticle capacity for *rh-s-ACE2i-biotin* between 60 and 90, consistent with what previously found with biotin ligands of similar molecular weight [19].

3.3. The affinity of rh-s-ACE2i-biotin for SARS-CoV-2 RBD is affected by its multimerization onto the ANANAS core

We investigated if and how the multimerization of ACE2 on the nanoparticles and the density of its packing affect its ability to recognize the Spike protein RBD. To this end, the interaction between *rh-s-ACE2i-biotin* and RBD was studied using an ELISA assay in which plate-immobilized RBD (Wuhan and Omicron: BA.1) was incubated with serial dilutions of *rh-s-ACE2i-biotin* in either monomeric form - as such or complexed with avidin (ACE2:avi = 1:1 mol:mole) - or multimerized onto ANANAS at different surface densities. Assemblies were tested at up to a maximum of 60 molecules/NP (ACE2:NP = 15, 30 and 60 mol:mole – ACE2:NP-R15, ACE2:NP-R30, ACE2:NP-R60), namely the highest molar ratio in solution which led to almost quantitative loading of the soluble protein onto the NP so that no need for purification to remove the unbound fraction was necessary prior to testing.

The results (Fig. 3) showed that, despite the presence of the C-terminal biotin tag and iodoacetamide thiol capping, *rh-s-ACE2i-biotin* maintains high affinity for RBD. The dissociation constants were in the nanomolar range (Wuhan: Kd = 1.34×10^{-9} M^{-1}, Omicron Kd = 6.57×10^{-9} M^{-1}, see also Table S1 in Supplementary Information, S.I.) in agreement with the literature [37]. Despite the documented higher infectivity of the Omicron variant, the affinity recorded for its RBD variant (BA.1) was almost 5 times lower than the original variant, in agreement with what measured by other authors through a reverse ELISA assay (plate-immobilized RBD added of serial dilution of ACE2) [38].

The *rh-s-ACE2i-biotin*: RBD interaction is negatively affected (Kd = 7.57×10^{-9} M – Wuhan RBD only) by complexation of *rh-s-ACE2i-biotin*

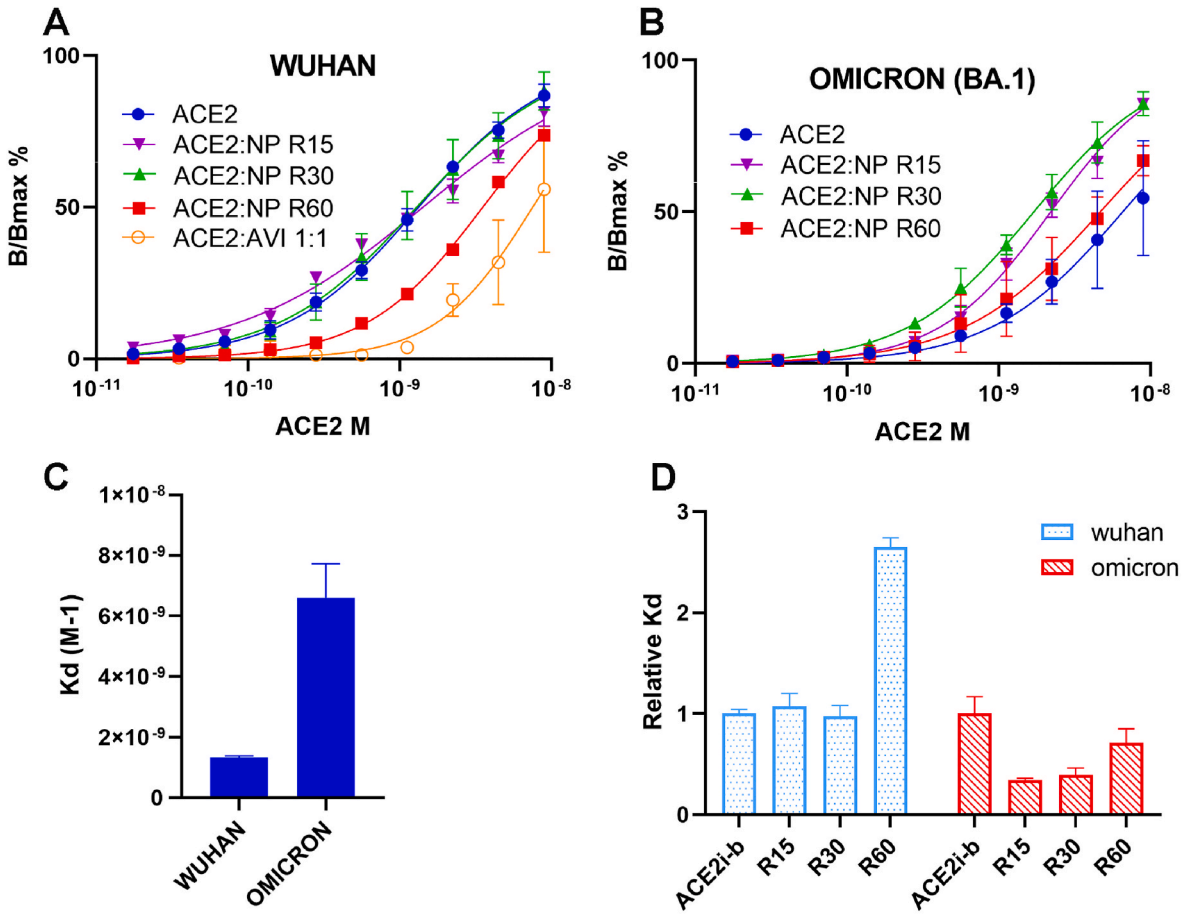

Fig. 3. Affinity of rh-*s*-ACE2-biotin in solution or multimerized onto the NP surface. Representative curves of binding to RBD of rh-*s*-ACE2-biotin in free form, and multimerized onto the surface of nanoparticles at ACE2:NPs molar ratios between 15:1 and 60:1 measured by ELISA; A) Wuhan, B) Omicron variants, C) dissociation constants calculated from the ELISA curves; D) dissociation constants of the *rh-s-ACE2i-biotin*:RBD interaction for ACE2i differently formulated relative to the protein in solution. An R value > 1 indicates lower affinity. Kds were computed using the GraphPad-Prism® software and the one site specific binding equation. Data indicate mean ± SD of 2–4 independent experiments each performed in duplicate. Full data are also reported in the Supplementary Information (S.I.) file (Table S1).

with monomeric avidin. This effect may be due to electrostatic repulsion, since both avidin [39] and RBD [40] are positively charged at neutral pH. Accordingly, this negative effect was not seen when *rh-s-ACEi-biotin* was complexed with the avidin in the nanoparticles, which have a net negative charge (in ANANAS the positive charge of avidin is neutralized by the nucleic acid of the nucleating plasmid).

More interestingly, the interaction is affected by the ACE2 packing density at the NP surface, with some differences and similarities amongst the two RBD variants. In the case of less densely packed ACE2:NP-R15 and ACE2:NP-R30 assemblies, the ACE2:RBD affinity was similar to that of the free molecule for the Wuhan variant, and higher for the BA.1 Omicron. Consistently for both RBDs, the highest ACE2 surface density tested (ACE2:NP-R60) showed the lowest affinity amongst the nanoassembled series.

3.4. *Rh-s-ACE2 inhibits SARS-CoV-2 infection more efficiently when multimerized onto the ANANAS core*

To test if and how any of the different ACE2:NP formulations exerted antiviral activity against the SARS-CoV-2 virus, we used the Wuhan variant of the virus and studied its infection in Calu-3 cells. Calu-3 is a human lung epithelial cell line that expresses both the ACE2 receptor and the TMPRSS2 cofactor on the cell membrane and, thereby, is susceptible to SARS-CoV-2 infection [3]. We incubated the SARS-CoV-2 virus with the recombinant biotinylated ACE2 (*rh-s-ACE2i-biotin*) or different ACE2:NP formulations for 10 min prior to infection of Calu-3 cells. Thirty h post infection, which is the time required for the virus to complete the first round of replication [41], we measured the amount of newly infectious viruses produced, using vehicle-treated virus as control. We used multiplicity of infection (MOI) of 0.1, which, in our assays corresponded to $2.75x10^3$ infectious particles. This assay allowed us to compare the viral progeny produced by a fixed number of infectious particles, treated or untreated with the soluble ACE2 or the ACE2:NP formulations, upon infection of Calu-3 cells. We measured to which level the soluble ACE2-or the ACE2:NP-treated virus impaired infection of human cells by measuring the amount of newly infectious virus produced after the first viral replication cycle, compared to vehicle-treated (control) virus.

First, we evaluated the inhibitory effect of increasing concentrations (0.025–2.5 μg/ml) of soluble *rh-s-ACE2i-biotin* on the SARS-CoV-2 infection of Calu-3 cells (Fig. 4A). Under these conditions, *rh-s-ACE2i-biotin* reduced the SARS-CoV-2 infectious cycle in a dose-dependent manner, reducing the viral titre by up to 33 % at the highest tested concentration (i.e. 2.5 μg/ml). These data are consistent with a recent report [6] and also in line with the ELISA results obtained when challenging the SARS-CoV-2 RBD with the *rh-s-ACE2i-biotin*. We further investigated the efficacy of the *rh-s-ACE2i-biotin* coupled to ANANAS nanoparticles in inhibiting the SARS-CoV-2 infectious cycle. We tested

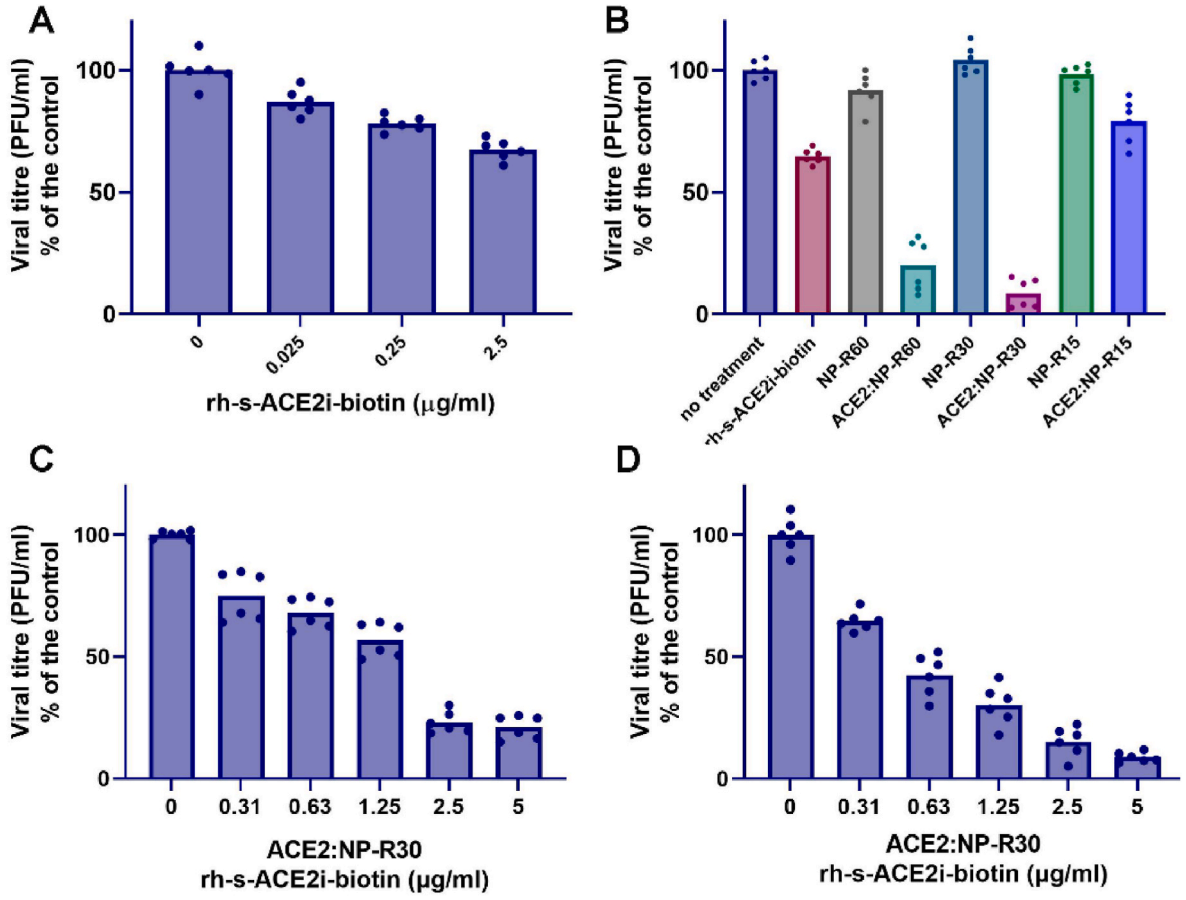

Fig. 4. Inhibition of SARS-CoV-2 infectivity by monomeric and nanoassembled rh-*s*-ACE2i-biotin. **A)** Inhibition of SARS-CoV-2 infection in Calu-3 by rh-*s*-ACE2i-biotin in monomeric form as a function of its concentration. Infection (Wuhan variant) was performed at MOI (multiplicity of infection) of 0.1. The virus was pre-incubated for 10 min with rh-*s*-ACE2i-biotin prior to Calu-3 cells infection; **B)** Efficacy of inhibition of SARS-CoV-2 infection (Wuhan variant) by rh-*s*-ACE2i-biotin at 2.5 μg/mL in monomeric or multimerized form on the ANANAS core at different ACE2:NP molar ratios. To keep the concentration of ACE2 in the assay constant at 2.5 μg/mL, the concentration in nanoparticles was different in the different samples (12.9, 25.7 and 51.5 μg/mL for ACE2:NP-R60, ACE2:NP-R30 and ACE2:NP-R15, respectively). Non-functionalized nanoparticles were therefore tested as control at these three concentrations, together with rh-*s*-ACE2i-biotin at 2.5 μg/mL in monomeric form; **C/D)** Efficiency in viral (Wuhan/Omicron Variants) cycle inhibition of increasing ACE2:NP-R30 concentrations (0–5 μg/ml). Bars indicate the mean of n = 2 biological replicates. Each condition was tested in triplicate per replicate. Individual data points are shown as dots.

different ACE2:NP ratios (i.e. 15, 30 and 60) and obtained a very strong viral inhibition when using ACE2:NP-R30, which displayed the best antiviral activity (91.5 % of virus reduction). Also ACE2:NP-R60 displayed a good potency, albeit less (80 % of virus reduction) than ACE2:NP-R30 (Fig. 4B).

Of note, *rh-s-ACE2i-biotin* multimerization on the ANANAS nanoparticles improved inhibition of the SARS-CoV-2 infection by about 10-fold, with respect to the use of the soluble monomeric protein. We observed no antiviral activity when we incubated core nanoparticles with the virus prior to viral infection, indicating that the antiviral effects depended on the presence of ACE2 on the surface of the ANANAS nanoparticles. We next measured the antiviral activity on both Wuhan and Omicron variants at increasing concentrations of ACE2:NP-R30 (Fig. 4C) up to a maximum 5 μg/mL in ACE2 titer and obtained a dose-dependent reduction. In the case of the Wuhan variant, the maximum efficacy was reached at 2.5 μg/mL, with no additional effect at higher concentrations (about 80 % inhibition at both 2.5 and 5.0 μg/mL). In case of the omicron Variant (Fig. 4D) the efficacy was slightly superior: the Omicron infectious cycle was hampered up to 92 % at the highest ACE2:NP-R30 dose tested, confirming the high antiviral potential of ANANAS coupled to the ACE2 receptor in the impairment of SARS-CoV-2 virus.

In parallel, we observed that the nanoparticles neither alone nor coupled to *rh-s-ACE2i-biotin* (at 30 and 60 ACE2:NP ratio) exhibited cytotoxic effects on human cells (Fig. S2 in S.I.), indicating that the observed antiviral effect depends on the effect of ACE2:NP on the SARS-CoV-2 virus.

We employed transmission electron microscopy (TEM) to directly visualize the effect exerted by the multimerized *rh-s-ACE2i-biotin* on the virus, (Fig. 5). To this end, nanoassemblies and virus were mixed in buffer at the same ratio as for the infection inhibition experiments. Samples were then treated with PFA to inactivate the virus and negatively stained with uranyl acetate. To confirm the identity of the polyavidin based nanoparticles a second staining with biotinylated gold nanoparticles (5 nm) was performed. The virus alone shows the expected circular membrane structure, with a diameter of about 90 nm, surrounded by S proteins. The ACE2:NP-R30 assemblies appear as toroids, in line with the shape of the 'core' NPs reported in the literature

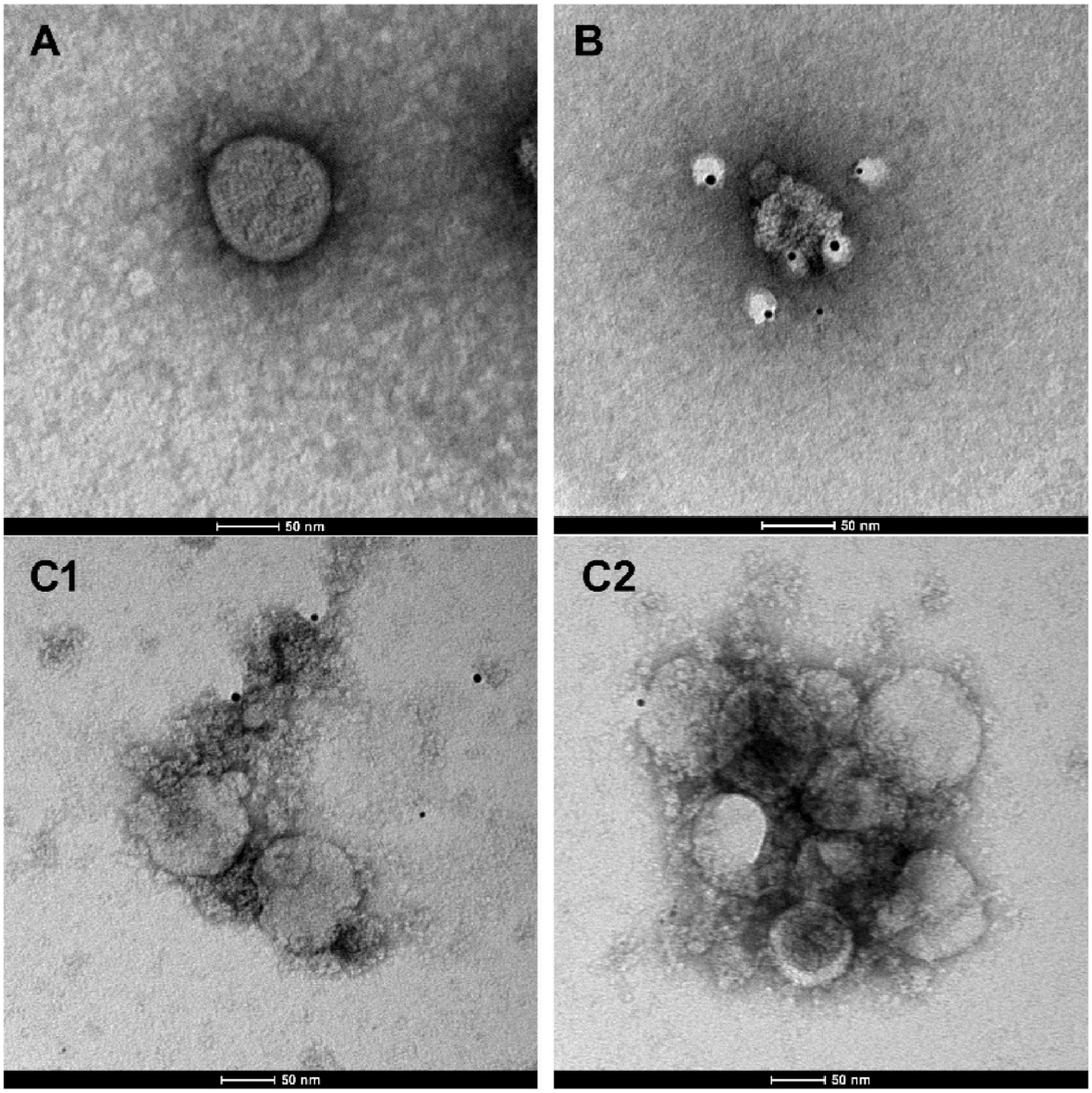

Fig. 5. Transmission Electron Microscopy. Representative images of **A)** SARS-CoV-2, **B)** the ANANAS:rh-*s*-ACEi2-30 (ACE2:NP-R30) nanoassembly and **C1/C2**) the mixture of SARS-CoV-2:ACE2:NP-R30 generated at PFU:NP molar ratio = 1:100. Samples were negatively stained with 1 % uranyl acetate, followed by biotin-nanogold (5 nm). The gold nanoparticles appear ad black dots. More images can be found in the Supplementary information file (Fig. S3).

[18]. The addition of 30 *rh-s-ACE2i-biotin* molecules did not noticeably change the appearance of the NPs, in agreement with the colloidal stability demonstrated by the DLS data (Fig. 2). The ACE2:NP-R30:virus mixture shows agglomerates in which several viral particles are "wrapped" within ANANAS-based multi-protein structures. Notably, the location of the NP:virus contact points are in line with the S protein distribution at the viral surface.

3.5. Nasal instillation of the ACE2:ANANAS allows efficient and long lasting pulmonary localization

In humans, the SARS-CoV-2 has a peculiar tropism for the airway epithelial cells expressing the ACE2. Therefore, inhalation of the ACE2:NP nanodecoy could allow fast interaction with the virus and, therefore, reduce the symptoms due to the infection. The potentials of this approach depend on the ability of the nanoparticles to flow along the airways, trespass the surfactant barrier, penetrate in the lung parenchyma, and interact with resident macrophages without inducing acute toxicity.

Based on these assumptions, we investigated the biodistribution of the nanoassemblies in healthy mice following nasal instillation by an ex vivo whole-organ measurement that furnishes a quantitative estimation of the ability of our formulations to reach the lungs. To this end, both ACE2:NP-R30 and non-functionalized ANANAS (ANANAS, used as controls) were fluorescently labelled by addition of biotin-C_6-alexa633 (10 % of total BBS) as a tracking agent (Fig. S4 in S.I.). Their biodistribution was monitored for up to 72 h after a single nasal instillation by measuring the fluorescence from lungs collected from mice sacrificed at different timepoints after treatment with the two formulations.

Fig. 6A shows the NPs' biodistribution in all selected organs after a single intranasal (i.n.) administration. The histograms of the NP-related fluorescent signal measured by IVIS (Fig. 6B) reveals that signal associated with the nanoparticles rapidly reached the lungs with a peak of concentration at 15 min after administration and fades away very

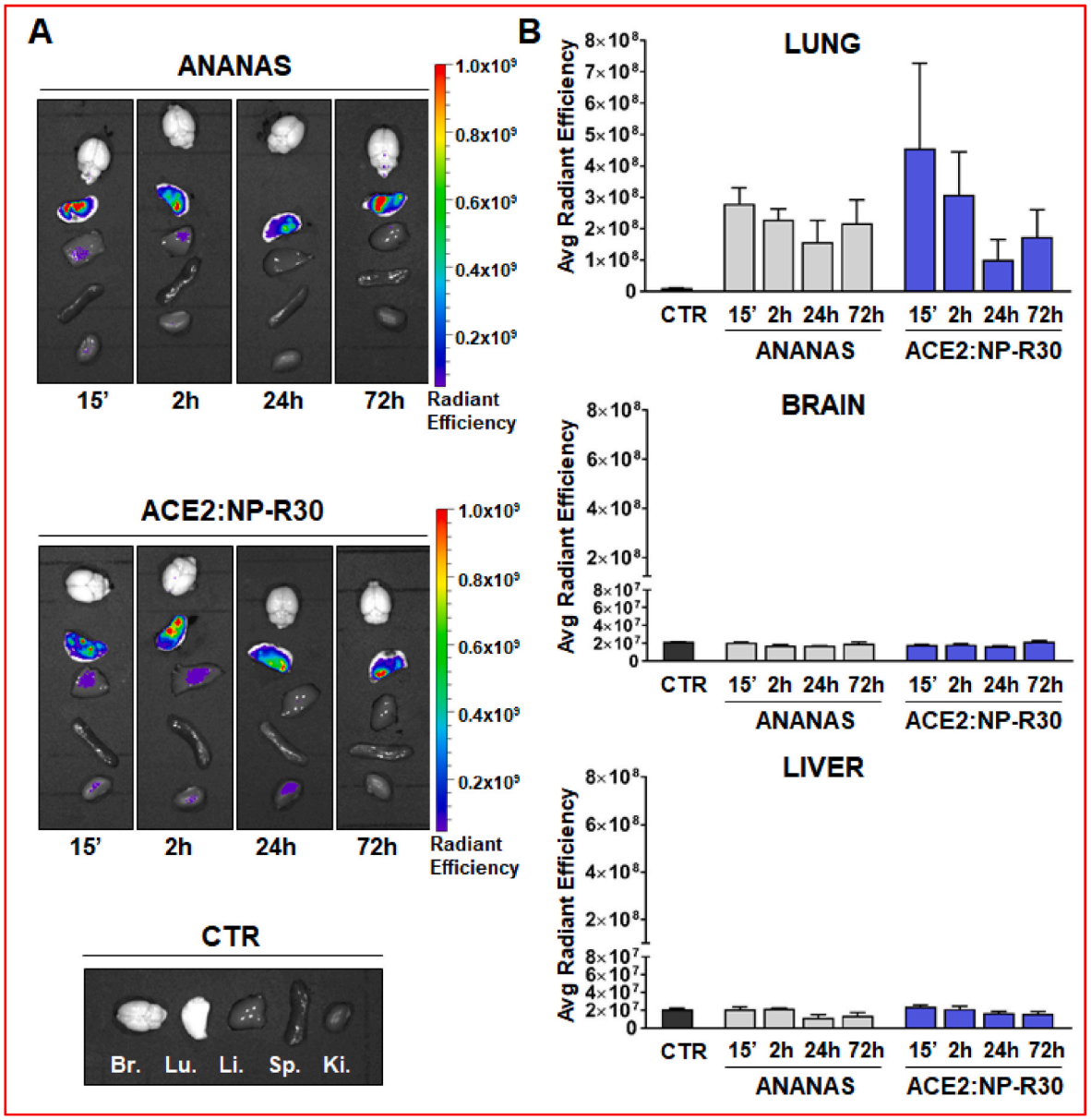

Fig. 6. Ex vivo imaging (A) Ex vivo optical imaging of excised organs from animals sacrificed 15′, 2 h, 24 h and 72 h after vehicle, ANANAS, and ACE2:NP-R30 administration. Br. = brain, Lu. = lungs, Li. = liver, Sp. = spleen, Ki. = kidneys. (B) Quantification of ex vivo optical imaging signal. Data are reported as mean ± SE. The data were analyzed by One-way ANOVA using Dunnet's test. *$p < 0.1$, **$p \leq 0.01$.

slowly, persisting for longer than 72 h. The fluorescence intensity registered in organs other than the lungs was about ten-fold lower, indicating that an almost selective tropism for this tissue can be obtained through this route of administration. A small but detectable signal was observed in the kidneys of animals treated with ACE2:NP-R30. The measurement by IVIS confirmed this trend (Fig. S5). However, confocal microscopy did not reveal an accumulation of ACE2:NP-R30 in kidney parenchyma thus suggesting a transient flux due to their excretion (Fig. S6).

Confocal microscopy images (Fig. 7) show that both formulations share the same pattern of penetration. The NP-associated signal (red) initially passes through the bronchioles, then spreads along the whole parenchyma, accumulates in the tissue macrophages (CD68 marker, green signal) and finally generates long lasting interaction with the alveolar vessels. A slight difference in the time-dependent pattern was observed between the groups. The ACE2 carrying nanoassemblies showed a faster and more extended distribution in the lung parenchyma, whereas the non-functionalized ones were up-taken from the macrophages more rapidly and had a more efficient passage in the endothelial cells. This could be due to the difference in the composition of the surfaces exposed by the two formulations.

The higher magnified images (Fig. 7, lower panel) show that the instilled nanoparticles localize in the bronchiolar area and rapidly penetrate the lung tissue. With time, a growing overlap of the NP related signal with that of the macrophages (yellow arrows) occurs, concurrent with progressive decrease of the NP-related signal in the lung parenchyma. Interestingly, at 72 h a particular localization of the Alexa633 (red) signal was found, which appears continuously distributed along the alveolar structures and at the periphery of the bronchioles, probably associated to NP degradation products. In fact, it is expected that once the protein-based ANANAS enter the lysosomes, they begin to lose their stability and to be proteolytically degraded. This process is likely to lead to progressive unravelling of the original NP structure and separation of the various NP components. The latter may be washed out of the tissue or captured by cell/tissue components, in any case changing their local environment. To investigate this phenomenon, we performed immunofluorescence staining of lung tissue samples from animals sacrificed 24h and 72h after inhalation with an anti-PEG antibody to visualize the biotin-PEG component of the core NPs (which is added for colloidal stabilization [17]). The results (Fig. S7) showed co-localization of biotin-C6-alexa633 and biotin-PEG at 24 h but not at 72 h post-administration, confirming that the NP structure was no longer

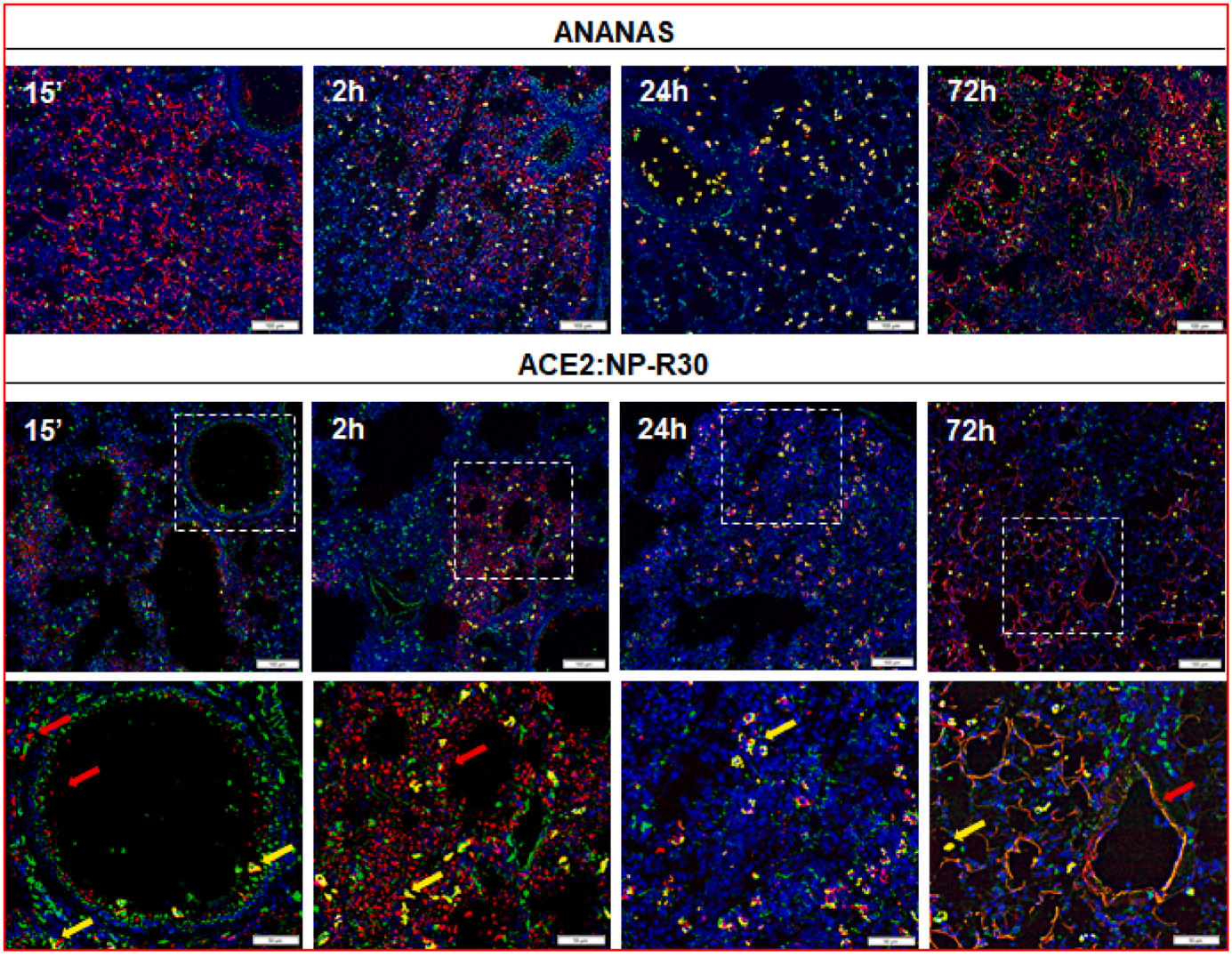

Fig. 7. Nanoparticles localization in tissues. Representative images of the tissue distribution of ANANAS or ACE2:NP-R30 in lungs 15′, 2, 24 and 72 h after treatment. The blue signal refers to the nuclei (Hoechst 33258 staining), green corresponds to the lysosomal component of macrophages (CD68 Antibody), red is associated with the alexa633 dye linked to the NPs, yellow corresponds to co-localized red and green signals. Scale bar = 100 μm. In the lower panel, representative images of higher magnification (15X) of lungs for each timepoint (yellow arrows: nanoparticles co-localized with macrophages, red arrows: nanoparticles alone). Scale bar = 50 μm. (For interpretation of the references to colour in this figure legend, the reader is referred to the Web version of this article.)

preserved at the latest time point. Notably, the loss of NP integrity may be responsible for the slight increase in the biotin-C6-alexa633-related signal observed by IVIS in the lung at 72 h (Fig. 6B), as it is known that the fluorescence of the dye is quenched when close to the ANANAS core [23] due to the presence of the aromatic amino acid residues within the avidin-biotin binding pocket.

3.6. Nanodecoy pulmonary localization shows no hallmarks of inflammation or toxicity

Fig. 8 shows representative images of the histopathological analysis of lung parenchyma processed with H&E from untreated mice or treated with ANANAS/ACE2:NP-R30 and sacrificed 15', and 2, 24, and 72 h after treatment. No relevant hallmarks of inflammation, alveolar damage or other tissue alterations were observed at all timepoints in the pathogen-free immunocompetent mice. No differences between sections from vehicle- and ANANAS/ACE2:NP-R30- treated animals were detected, ruling out treatment-related pathological changes. The same profile of safety was observed in kidneys (Fig. S8)

ANANAS contain a non-coding plasmid DNA of bacterial origin, and therefore its unmethylated CpG sequences, even if masked by the avidin tightly bound to the nucleic acid, could potentially be recognized by TLR9 and activate the NF-κB mediated pro-inflammatory pathway [42]. To rule out this possibility, the levels of several pro-inflammatory cytokines (IFN-γ and TNFα) and an anti-inflammatory cytokine (IL-10) were measured using an AlphaLISA assay (Fig. 9). Neither nanoformulations induced relevant changes in the cytokine levels compared to the untreated mice.

4. Discussion

The possibility of using a protein-based nanoparticle system to generate an effective semisynthetic multimeric ACE2 nanodecoy capable of preventing SARS-CoV-2 infection was demonstrated. Efficacy was achieved without the use of a lipid membrane for receptor anchorage, as otherwhise necessary in vesicle-based nanodecoys.

In our conditions, the optimized assembly was able to prevent 80–90 % of infectivity within a few minutes of viral contact at ACE2 nanomolar concentration and with more than 10-fold higher efficacy than the soluble protein. The fact that efficacy is maintained throughout both Wuhan and Omicron variants confirms that this approach can bypass virus mutations and suggests that this strategy could be a valid add-on to the use of monoclonal antibodies.

By taking advantage of the ease of composition modulation allowed by this nanotechnology platform we were able to screen composition/efficacy relationships. Indeed, while the use of ACE2 multimer-based nanodecoys and their effectiveness in inhibiting/preventing viral infections has already been demonstrated in the literature using a number of nanoparticle geometries [43], as of today there was no indication as to if and to which extent receptor density at the nanoparticle surface affects efficacy. This is a fundamental information in case one seeks to bring the semisynthetic nanodecoy product towards clinical translation.

To study composition/function relationships using this polyavidin platform, it is necessary to use well-defined monomeric biotinylated building blocks. In our hands, the recombinant ACE2 ectodomain produced following established protocols [30,32] did not fulfill this requirement, both because it proved to be hard to biotinylate by chemical means and for its instability to disulfide–driven polymerization. Aggregation occurred even though this fragment does not to contain the ferredoxin-like fold domain (a.k.a., Neck-domain) that determines dimerization of the native receptor at the cell membrane [44]. However, the recombinant ACE2 ectodomain produced contains two free cysteine residues partially exposed to the protein surface (i.e., Cys261 and Cys498, Fig. S1 in S.I. file), which likely drive this process. Since information on rh-*s*-ACE2-biotin conjugates commercially available did not guarantee the absence of multimers, we decided to carry out enzymatic biotinylation and 'block' the recombinant product cysteines along the purification step by iodoacetamide. This strategy proved to be effective, as *rh-s-ACE2i-biotin*, besides being stable as a monomer, also maintained high affinity for the RBD..

Pre-formulation studies demonstrated that a) the *rh-s-ACE2i-biotin* can be tethered efficiently to ANANAS, b) the ACE2:NP assemblies are colloidally stable and c) each nanoparticle can accommodate more than 60 ACE2i-biotin units. However, the data also indicate that above the ACE2:NP molar ratio of 30 it is difficult for the biotin-protein to reach the nanoparticles surface, likely because of some crowding effect. In line

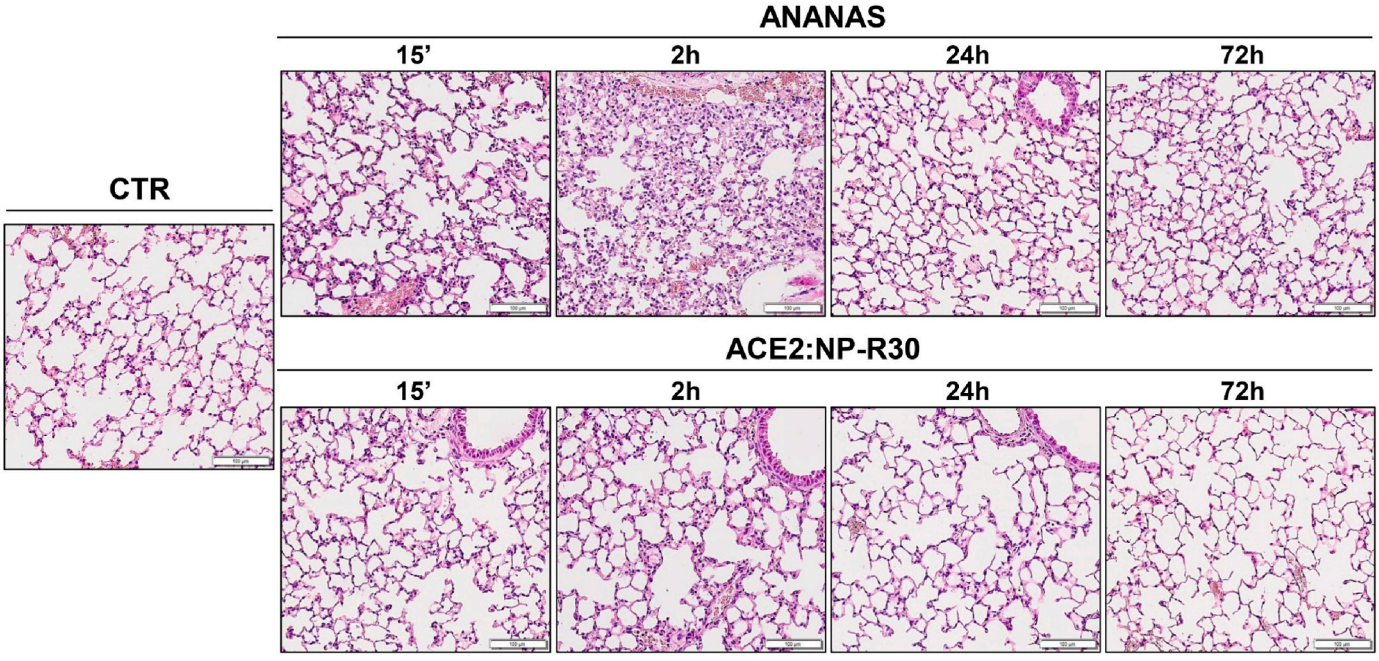

Fig. 8. Histological evaluation by hematoxylin and eosin staining of lung tissue of mice treated with vehicle (CTR), ANANAS and ACE2:NP-R30 and sacrificed 15′, 2, 24, and 72 h after the treatment. Scale bar = 100 μm.

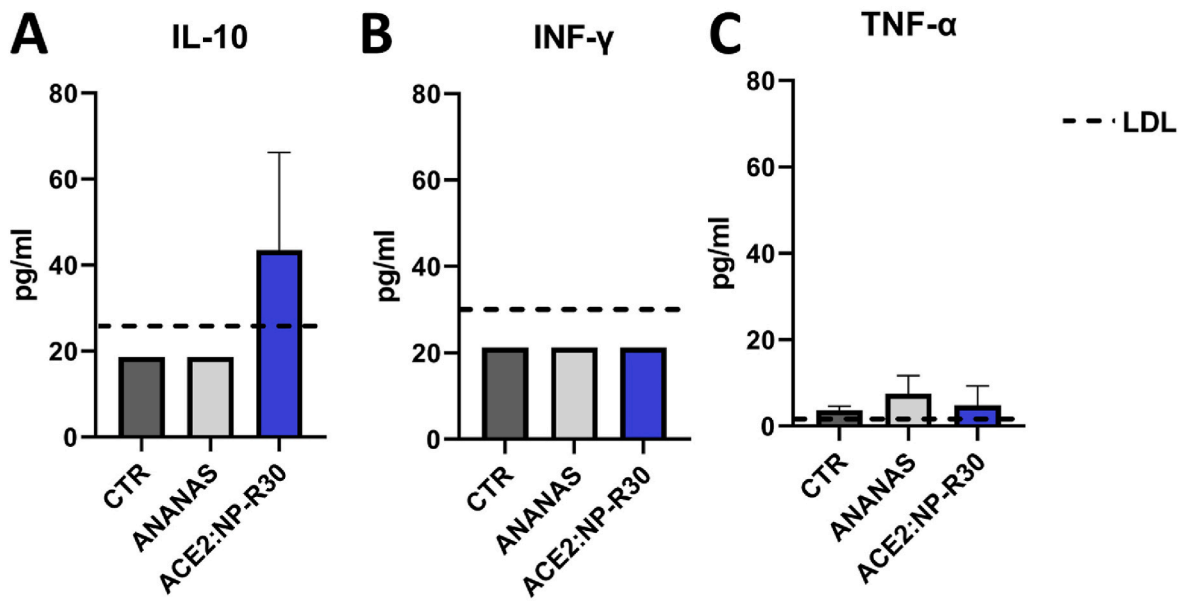

Fig. 9. Cytokine analysis in serum of untreated and treated animals. (A) IL-10, (B) INF-γ, and (C) TNF-α concentrations were measured in serum samples from treated animals and controls 72h after ANANAS or ACE2:NP-R30 administration. LDL = low detection limit. Data are reported as mean±SD. Statistical analysis was performed by One-way ANOVA, followed by Tukey post-hoc test. No differences were found comparing ANANAS or ACE2:NP-R30 with CTR mice, or directly comparing the two nanoformulations. Overall, these data indicate that the intranasal administration of these formulations to healthy mice does not stimulate an inflammatory response at least over the period of our analysis (72 h), confirming the evidence of lack of toxicity.

with this interpretation, while the loading test performed at ACE2:NP ratio in solution = 90 revealed that at least 71 *rh-s-ACE2i-biotin* molecules can be linked to the NPs, at ACE2:NP ratio of 60, about 10 % of the rh-*s*-ACEi-biotin molecules remained in solution. The fact that non-quantitative binding of *rh-s-ACE2i-biotin* occurs at ACE2:NP > 30 when below the saturation limit suggests some difficulty in the avidin/biotin interaction at high *rh-s-ACE2i-biotin* packing densities. This is probably due to the relatively short BAP spacer between the protein and biotin moieties. Previous work describing the use of the ANANAS platform always showed quantitative binding of relatively bulky biotinylated moieties (e.g. proteins, polymers and peptides [19,21,22]) when added below their saturation limit. In these cases, the spacer between the biotin and the cargo was always a long (5 kDa) PEG spacer, which is likely to allow efficient spacing of molecules around the NP core. It is possible that the short BAP spacer does not permit efficient spacing between the different *rh-s-ACE2i-biotin* units and therefore "forces" them to bind to the nanoparticle with a 'rigid' configuration. This would imply that above a certain surface density, ACE2 packing would occur without changing the thickness of the monolayer and, therefore, the hydrodynamic volume. This is consistent with the finding that no increase in size was registered by DLS between ACE2:NP 30 and 60, despite both gel permeation chromatography and zeta potential measurements indicated an increase in loading.

Even more importantly, our infectivity studies clearly showed that a) ACE2 density at the nanodecoy surface does make the difference and b) there is no univocal correlation between ligand surface packing and efficacy. In fact, in the antiviral tests ACE2:NP-R30 outperformed both the more and less densely packed R60 and R15 assemblies.

To understand whether affinity or avidity issues are responsible for these differences we compared the infectivity data with the affinity information gathered by ELISA. Both assays suggest that excessive ACE2 surface density has a negative impact on potency. In fact, the R60 assembly was less effective than the R30 in preventing viral infection and the affinity for RBD of the ACE2i assembled on it was less than when assembled at R30. This negative effect could be due to a distortion of the protein conformation due to excessive surface crowding, in agreement with the rigid conformation hypothesis derived from the pre-formulation studies. On the other hand, while the ACE2i:RBD affinity was similar when the ACE2i ligand was assembled at the R15 and R30 ratios, ACE2:NP-R15 proved to be much less effective than ACE2:NP-R30 from the point of view of the antiviral activity. This fact cannot be explained with affinity or crowding effects and suggests that there is a geometric/spatial requirement for optimal interaction of the virus surface with the multimerized ACE2i nanodecoy. In this respect, the number of spikes/virion (Wuhan) is about 27, with a surface density of 1 molecule/1000 nm^2 [45]. Earlier works have shown that the surface area onto the ANANAS nanoparticles available for binding biotinylated macromolecules is dictated by steric factors and is of about 6000 nm^2 [19]. Therefore, 30ACE2i/assembly correspond to a surface density of about 1 molecule/200 nm^2. Accordingly, a Spike:ACE2 surface ratio of 1:10 (corresponding to a 1:1 molar ratio) seems to guarantee the optimal geometry for efficacy.

It should be noted that the ANANAS nanoparticles primarily display a toroidal shape, which derives from the condensation of a circular plasmid DNA [18]. The coiling of this DNA promoted by the adsorption of avidin is the most favored energetically; however, other more extended shapes are possible (see also S.I.), particularly if there is an energy gain. For example, this may occur when ligand-decorated (e.g. ACE2i) nanoparticles are exposed to surfaces covered with ligand baits (e.g. the S protein on SARS-CoV-2 or the RBD decorated ELISA plate). Indeed, in the virus/ACE2:NP-R30 mixtures shown by the TEM images the nanoparticles appear as partially uncoiled filaments surrounding the virus. It is possible that in the presence of the virus the ACE2:toroidal nanoparticle disentangles and wraps around it with the ACE2 moieties interacting with the S protein. Accordingly, the possibility to engulf all S proteins (and therefore act as effective decoy) depends on the distance between the ACE2 moieties, justifying the spatial requirement observed experimentally.

While the overall data suggest that when both ligand and receptor are immobilized on solid surfaces, there is a relationship between the two elements spatial organization and recognition efficacy, the question remains as to *whether the relationship identified with the ACE2-ANANAS: SARS-CoV-2 system can be of general value* and can be transferred also to other multimeric nanodecoys. In fact, it is likely that the geometry (e.g. curvature radius) of the nanodecoy and its composition (e.g. lipid membrane vs polymer/protein interface) may play additional roles.

Therefore, even if we could expect that ACE2 surface density may affect the potency of all ACE2 based nanodecoys, nanoparticles with geometries/compositions different than ANANAS may respond to different composition/efficacy rules.

The *in vivo* biodistribution and preliminary toxicology studies demonstrated that the ACE2:NP-R30 is safe and is capable of reaching the deep lung very rapidly by a simple inhalation. Its antiviral efficacy *in vivo* can depend on the ability of the nanoparticles to reach locations where the virus preferentially localizes, namely the lung parenchyma and its macrophages, which are at the forefront of the host immune-defense. Although *in vivo* efficacy studies are necessary, given the rapidity with which the assemblies reach the parenchyma and the slow removal by the macrophages, it is reasonable to assume that they could provide protection against viral invasion, similar to other ACE2 multimer nanodecoys described in the literature that had shown similar efficacy *in vitro*. Another question is *how long this protection would* last after inhalation. The fluorescence signal associated with the assembly remains in the lungs for up to 72 h. However, while at 2 h and 24 h the histology data clearly show that the NPs are present in both the parenchyma and macrophages, at the late time point analyzed (72 h) the fluorescent signal is more likely due to NP degradation products, which may no longer be active. As a general methodological note, it is important to recognize that the sole organ fluorescent intensity data may not be sufficient to predict the duration of efficacy and should be complemented by sub-localization studies to ascertain the nanoparticles fate.

5. Conclusions

We herein showed that the optimized semisynthetic protein-based ACE2:ANANAS assembly is a potent tool capable to counteract SARS-CoV-2 infection. The combined *in vitro*, biodistribution and preliminary toxicity data suggest that ANANAS based nanodecoys can be administered by inhalation and may provide protection from infection for at least 2–24 h, without acute toxic effects.

The poly-avidin platform used here is versatile and rapidly scalable. In principle, it could be easily adapted to generate nanodecoys against other viruses. With its safety profile demonstrated also in other contexts, its versatility and ease of preparation, this platform could become a useful tool to counteract pandemics and complement other preventive/pharmacological approaches.

From a more general perspective, the results demonstrate that semisynthetic nanoparticles lacking a fluid lipid-based membrane for receptor anchorage can be used as scaffolds to generate antiviral nanodecoys. In addition, we showed that the density of the recognition element at the decoy surface is important in defining its efficacy, suggesting that this parameter should be monitored along the optimization of any decoy systems, independently of the scaffold employed for receptor multimerization.

Author contribution

Conceptualization MM, SR, GPR, PB, MBV; Data curation SB, IF, MBV, SF, VB; Formal analysis SB, IF; Funding acquisition: MM, GPR, SR, MB, AnM, FF; Investigation SB, IF, SF, AnnM, GYM, ES, AP, AC, LP; Methodology: MM, SR, SB, IF, FF; Project administration MM, SR, FF, PB; Resources: MM, SR, PB, FF; Supervision: MM, SR, FF, PB; Visualization: MM, SR, SB, IF; Writing – original draft: MM, SR, IF; Writing review &; editing MM, SR, FF, SR, MB, MBV, PB.

Declaration of competing interest

The authors declare that they have no known competing financial interests or personal relationships that could have appeared to influence the work reported in this paper.

Data availability

No data was used for the research described in the article.

Acknowledgements

Research at UNIPD was supported by Fondazione Compagnia San Paolo (Project no B/2020/0138 - *Innovative treatment options to inhibit SARS-CoV2 infection and treat COVID-19 patients (INTENTION);* ANANAS dilution buffer, biotin HRP were a kind gift of ANANAS nanotech; Research in the FF lab at UNIPV, in the SNR lab at UNIPD and at the Mario Negri Institute was also supported by EU funding within the NextGenerationEU-MUR PNRR Extended Partnership initiative on Emerging Infectious Diseases (Project no. PE00000007, INF-ACT), by the Italian Ministry of Health (Piano Operativo Salute, IMMUNO-HUB project to FF), by the Armenise Harvard Foundation (CDA 2013 to FF), by the NATO Science for Peace and Security Program (SPS5701 to FF), and by the Italian Association for Cancer Research (grants MFAG 20075 and Bridge 27004 to FF; grant IG 21850 to SNR).

We are grateful to Dr. Federico Caicci for support in TEM imaging. The following reagents were produced under HHSN272201400008C and obtained through BEI Resources, NIAID, NIH: Vector pCAGGS Containing the SARS-Related Coronavirus 2, Wuhan-Hu-1 Spike Glycoprotein Receptor Binding Domain (RBD), NR-52309.

Appendix A. Supplementary data

Supplementary data to this article can be found online at https://doi.org/10.1016/j.biomaterials.2023.122394.

References

[1] X. Wei, G. Zhang, D. Ran, N. Krishnan, R.H. Fang, W. Gao, S.A. Spector, L. Zhang, T-Cell-Mimicking nanoparticles can neutralize HIV infectivity, Adv. Mater. 30 (2018), https://doi.org/10.1002/adma.201802233.

[2] G.L. Hendricks, K.L. Weirich, K. Viswanathan, J. Li, Z.H. Shriver, J. Ashour, H. L. Ploegh, E.A. Kurt-Jones, D.K. Fygenson, R.W. Finberg, J.C. Comolli, J.P. Wang, Sialylneolacto-N-tetraose c (LSTc)-bearing liposomal decoys capture influenza a virus, J. Biol. Chem. 288 (2013) 8061–8073, https://doi.org/10.1074/jbc.M112.437202.

[3] M. Hoffmann, H. Kleine-Weber, S. Schroeder, N. Krüger, T. Herrler, S. Erichsen, T. S. Schiergens, G. Herrler, N.H. Wu, A. Nitsche, M.A. Müller, C. Drosten, S. Pöhlmann, SARS-CoV-2 cell entry depends on ACE2 and TMPRSS2 and is blocked by a clinically proven protease inhibitor, Cell 181 (2020) 271–280.e8, https://doi.org/10.1016/j.cell.2020.02.052.

[4] K. Kuba, Y. Imai, S. Rao, H. Gao, F. Guo, B. Guan, Y. Huan, P. Yang, Y. Zhang, W. Deng, L. Bao, B. Zhang, G. Liu, Z. Wang, M. Chappell, Y. Liu, D. Zheng, A. Leibbrandt, T. Wada, A.S. Slutsky, D. Liu, C. Qin, C. Jiang, J.M. Penninger, A crucial role of angiotensin converting enzyme 2 (ACE2) in SARS coronavirus-induced lung injury, Nat. Med. 11 (2005) 875–879, https://doi.org/10.1038/nm1267.

[5] I. Caputo, B. Caroccia, I. Frasson, E. Poggio, S. Zamberlan, M. Morpurgo, T. M. Seccia, T. Calì, M. Brini, S.N. Richter, G.P. Rossi, Angiotensin II promotes SARS-CoV-2 infection via upregulation of ACE2 in human bronchial cells, Int. J. Mol. Sci. 23 (2022) 5125, https://doi.org/10.3390/ijms23095125.

[6] V. Monteil, H. Kwon, P. Prado, A. Hagelkrüys, R.A. Wimmer, M. Stahl, A. Leopoldi, E. Garreta, C. Hurtado del Pozo, F. Prosper, J.P. Romero, G. Wirnsberger, H. Zhang, A.S. Slutsky, R. Conder, N. Montserrat, A. Mirazimi, J.M. Penninger, Inhibition of SARS-CoV-2 infections in engineered human tissues using clinical-grade soluble human ACE2, Cell 181 (2020) 905–913.e7, https://doi.org/10.1016/j.cell.2020.04.004.

[7] A. Zoufaly, M. Poglitsch, J.H. Aberle, W. Hoepler, T. Seitz, M. Traugott, A. Grieb, E. Pawelka, H. Laferl, C. Wenisch, S. Neuhold, D. Haider, K. Stiasny, A. Bergthaler, E. Puchhammer-Stoeckl, A. Mirazimi, N. Montserrat, H. Zhang, A.S. Slutsky, J. M. Penninger, Human recombinant soluble ACE2 in severe COVID-19, Lancet Respir. Med. 8 (2020) 1154–1158, https://doi.org/10.1016/S2213-2600(20)30418-5.

[8] J. Kim, A. Jozic, A. Mukherjee, D. Nelson, K. Chiem, M.S.R. Khan, J.B. Torrelles, L. Martinez-Sobrido, G. Sahay, Rapid generation of circulating and mucosal decoy human ACE2 using mRNA nanotherapeutics for the potential treatment of SARS-CoV-2, Adv. Sci. (2022), https://doi.org/10.1002/advs.202202556.

[9] Y. Higuchi, T. Suzuki, T. Arimori, N. Ikemura, E. Mihara, Y. Kirita, E. Ohgitani, O. Mazda, D. Motooka, S. Nakamura, Y. Sakai, Y. Itoh, F. Sugihara, Y. Matsuura, S. Matoba, T. Okamoto, J. Takagi, A. Hoshino, Engineered ACE2 receptor therapy overcomes mutational escape of SARS-CoV-2, Nat. Commun. 12 (2021), https://doi.org/10.1038/s41467-021-24013-y.

[10] L. Zhang, S. Dutta, S. Xiong, M. Chan, K.K. Chan, T.M. Fan, K.L. Bailey, M. Lindeblad, L.M. Cooper, L. Rong, A.F. Gugliuzza, D. Shukla, E. Procko, J. Rehman, A.B. Malik, Engineered ACE2 decoy mitigates lung injury and death induced by SARS-CoV-2 variants, Nat. Chem. Biol. 18 (2022) 342–351, https://doi.org/10.1038/s41589-021-00965-6.

[11] A. Glasgow, J. Glasgow, D. Limonta, P. Solomon, I. Lui, Y. Zhang, M.A. Nix, N. J. Rettko, S. Zha, R. Yamin, K. Kao, O.S. Rosenberg, J.v. Ravetch, A.P. Wiita, K. K. Leung, S.A. Lim, X.X. Zhou, T.C. Hobman, T. Kortemme, J.A. Wells, Engineered ACE2 receptor traps potently neutralize SARS-CoV-2, Proc. Natl. Acad. Sci. USA 117 (2020) 28046–28055, https://doi.org/10.1073/pnas.2016093117.

[12] F. Xie, P. Su, T. Pan, X. Zhou, H. Li, H. Huang, A. Wang, F. Wang, J. Huang, H. Yan, L. Zeng, L. Zhang, F. Zhou, Engineering extracellular vesicles enriched with palmitoylated ACE2 as COVID-19 therapy, Adv. Mater. 33 (2021), https://doi.org/10.1002/adma.202103471.

[13] L. Rao, S. Xia, W. Xu, R. Tian, G. Yu, C. Gu, P. Pan, Q.-F. Meng, X. Cai, D. Qu, L. Lu, Y. Xie, S. Jiang, X. Chen, Decoy nanoparticles protect against COVID-19 by concurrently adsorbing viruses and inflammatory cytokines , (n.d.). https://doi.org/10.1073/pnas.2014352117/-/DCSupplemental.

[14] H. Zhang, W. Zhu, Q. Jin, F. Pan, J. Zhu, Y. Liu, L. Chen, J. Shen, Y. Yang, Q. Chen, Z. Liu, Inhalable nanocatchers for SARS-CoV-2 inhibition , (n.d.). https://doi.org/10.1073/pnas.2102957118/-/DCSupplemental.

[15] L. El-Shennawy, A.D. Hoffmann, N.K. Dashzeveg, K.M. McAndrews, P.J. Mehl, D. Cornish, Z. Yu, V.L. Tokars, V. Nicolaescu, A. Tomatsidou, C. Mao, C.J. Felicelli, C.F. Tsai, C. Ostiguin, Y. Jia, L. Li, K. Furlong, J. Wysocki, X. Luo, C.F. Ruivo, D. Batlle, T.J. Hope, Y. Shen, Y.K. Chae, H. Zhang, V.S. LeBleu, T. Shi, S. Swaminathan, Y. Luo, D. Missiakas, G.C. Randall, A.R. Demonbreun, M.G. Ison, R. Kalluri, D. Fang, H. Liu, Circulating ACE2-expressing extracellular vesicles block broad strains of SARS-CoV-2, Nat. Commun. 13 (2022), https://doi.org/10.1038/s41467-021-27893-2.

[16] C. Wang, S. Wang, Y. Chen, J. Zhao, S. Han, G. Zhao, J. Kang, Y. Liu, L. Wang, X. Wang, Y. Xu, S. Wang, Y. Huang, J. Wang, J. Zhao, Membrane nanoparticles derived from ACE2-rich cells block SARS-CoV-2 infection, ACS Nano 15 (2021) 6340–6351, https://doi.org/10.1021/acsnano.0c06836.

[17] M. Pignatto, N. Realdon, M. Morpurgo, Optimized avidin nucleic acid nanoassemblies by a tailored PEGylation strategy and their application as molecular amplifiers in detection, Bioconjugate Chem. 21 (2010) 1254–1263, https://doi.org/10.1021/bc100044u.

[18] M. Morpurgo, A. Radu, E.A. Bayer, M. Wilchek, DNA condensation by high-affinity interaction with avidin, J. Mol. Recogn. 17 (2004) 558–566, https://doi.org/10.1002/jmr.689.

[19] M. Morpurgo, S. Facchin, M. Pignatto, D. Silvestri, E. Casarin, N. Realdon, Characterization of multifunctional nanosystems based on the avidin-nucleic acid interaction as signal enhancers in immuno-detection, Anal. Chem. 84 (2012) 3433–3439, https://doi.org/10.1021/ac300276u.

[20] M. Morpurgo, A. Buda, S. Facchin, E. Dassie, E. Casarin, M.A. Jepson, H. Neumann, S. Realdon, G. Hatem, R. D'inca', G.C. Sturniolo, Detection of a fluorescent-labeled avidin-nucleic acid nanoassembly by confocal laser endomicroscopy in the microvasculature of& nbsp;chronically inflamed intestinal mucosa, Int. J. Nanomed. 10 (2015) 399, https://doi.org/10.2147/IJN.S70153.

[21] S. Facchin, L. Digiglio, R. D'Incà, E. Casarin, E. Dassie, M. Dettin, A. Zamuner, A. Buda, M. De Boni, D. Della Libera, A. D'Urso, G.C. Sturniolo, M. Morpurgo, Discrimination between ulcerative colitis and Crohn's disease using phage display identified peptides and virus-mimicking synthetic nanoparticles, Nanomedicine 13 (2017) 2027–2036, https://doi.org/10.1016/j.nano.2017.04.007.

[22] P. Bigini, S. Previdi, E. Casarin, D. Silvestri, M.B. Violatto, S. Facchin, L. Sitia, A. Rosato, G. Zuccolotto, N. Realdon, F. Fiordaliso, M. Salmona, M. Morpurgo, In vivo fate of avidin-nucleic acid nanoassemblies as multifunctional diagnostic tools, ACS Nano 8 (2014) 175–187, https://doi.org/10.1021/nn402669w.

[23] F. Roncato, F. Rruga, E. Porcù, E. Casarin, R. Ronca, F. Maccarinelli, N. Realdon, G. Basso, R. Alon, G. Viola, M. Morpurgo, Improvement and extension of anti-EGFR targeting in breast cancer therapy by integration with the Avidin-Nucleic-Acid-Nano-Assemblies, Nat. Commun. 9 (2018), https://doi.org/10.1038/s41467-018-06602-6.

[24] M. Bruna Violatto, E. Casarin, L. Talamini, L. Russo, S. Baldan, C. Tondello, M. Messmer, E. Hintermann, A. Rossi, A. Passoni, R. Bagnati, S. Biffi, C. Toffanin, S. Gimondi, S. Fumagalli, M.-G. De Simoni, D. Barisani, M. Salmona, U. Christen, P. Invernizzi, P. Bigini, M. Morpurgo, Dexamethasone conjugation to biodegradable avidin-nucleic-acid-nano-assemblies promotes selective liver targeting and improves therapeutic efficacy in an autoimmune hepatitis murine model article, ACS Nano 13 (2019) 4410–4423, https://doi.org/10.1021/acsnano.8b09655.

[25] M.O. Bubb, F. Green, J.D. Conradie, B. Tchernyshev, E.A. Bayer, M. Wilchek, Natural antibodies to avidin in human serum, Immunol. Lett. 35 (1993) 277–280, https://doi.org/10.1016/0165-2478(93)90194-7.

[26] F. Petronzelli, A. Pelliccia, A.M. Anastasi, R. Lindstedt, S. Manganello, L.E. Ferrari, C. Albertoni, B. Leoni, A. Rosi, V. D'Alessio, K. Deiana, G. Paganelli, R. De Santis, Therapeutic use of avidin is not hampered by antiavidin antibodies in humans, Cancer Biother. Radiopharm. 25 (2010) 563–570, https://doi.org/10.1089/cbr.2010.0797.

[27] Y. Fan, X. Li, L. Zhang, S. Wan, L. Zhang, F. Zhou, SARS-CoV-2 Omicron variant: recent progress and future perspectives, Signal Transduct. Targeted Ther. 7 (2022) 141, https://doi.org/10.1038/s41392-022-00997-x.

[28] D.-Y. Chen, C.V. Chin, D. Kenney, A.H. Tavares, N. Khan, H.L. Conway, G. Liu, M. C. Choudhary, H.P. Gertje, A.K. O'Connell, S. Adams, D.N. Kotton, A. Herrmann, A. Ensser, J.H. Connor, M. Bosmann, J.Z. Li, M.U. Gack, S.C. Baker, R. N. Kirchdoerfer, Y. Kataria, N.A. Crossland, F. Douam, M. Saeed, Spike and nsp6 are key determinants of SARS-CoV-2 Omicron BA.1 attenuation, Nature 615 (2023) 143–150, https://doi.org/10.1038/s41586-023-05697-2.

[29] M. Bruni, V. Cecatiello, A. Diaz-Basabe, G. Lattanzi, E. Mileti, S. Monzani, L. Pirovano, F. Rizzelli, C. Visintin, G. Bonizzi, M. Giani, M. Lavitrano, S. Faravelli, F. Forneris, F. Caprioli, P.G. Pelicci, G. Natoli, S. Pasqualato, M. Mapelli, F. Facciotti, Persistence of anti-SARS-CoV-2 antibodies in non-hospitalized COVID-19 convalescent Health care workers, J. Clin. Med. 9 (2020) 3188, https://doi.org/10.3390/jcm9103188.

[30] K.K. Chan, D. Dorosky, P. Sharma, S.A. Abbasi, J.M. Dye, D.M. Kranz, A.S. Herbert, E. Procko, Engineering human ACE2 to optimize binding to the spike protein of SARS coronavirus 2, Science 369 (1979) 1261–1265, https://doi.org/10.1126/science.abc0870, 2020.

[31] V. Verma, C. Kaur, P. Grover, A. Gupta, V.K. Chaudhary, Biotin-tagged proteins: reagents for efficient ELISA-based serodiagnosis and phage display-based affinity selection, PLoS One 13 (2018), e0191315, https://doi.org/10.1371/journal.pone.0191315.

[32] S. Faravelli, M. Campioni, M. Palamini, A. Canciani, A. Chiapparino, F. Forneris, Optimized recombinant production of secreted proteins using human embryonic kidney (HEK293) cells grown in suspension, Bio Protoc 11 (2021), https://doi.org/10.21769/BioProtoc.3998.

[33] M.A. Ramakrishnan, Determination of 50% endpoint titer using a simple formula, World J. Virol. 5 (2016) 85, https://doi.org/10.5501/wjv.v5.i2.85.

[34] D. Beckett, E. Kovaleva, P.J. Schatz, A minimal peptide substrate in biotin holoenzyme synthetase-catalyzed biotinylation, Protein Sci. 8 (1999) 921–929, https://doi.org/10.1110/ps.8.4.921.

[35] C.A. O'Callaghan, M.F. Byford, J.R. Wyer, B.E. Willcox, B.K. Jakobsen, A. J. McMichael, J.I. Bell, BirA enzyme: production and application in the study of membrane receptor–ligand interactions by site-specific biotinylation, Anal. Biochem. 266 (1999) 9–15, https://doi.org/10.1006/abio.1998.2930.

[36] P. Han, C. Su, Y. Zhang, C. Bai, A. Zheng, C. Qiao, Q. Wang, S. Niu, Q. Chen, Y. Zhang, W. Li, H. Liao, J. Li, Z. Zhang, H. Cho, M. Yang, X. Rong, Y. Hu, N. Huang, J. Yan, Q. Wang, X. Zhao, G.F. Gao, J. Qi, Molecular insights into receptor binding of recent emerging SARS-CoV-2 variants, Nat. Commun. 12 (2021) 6103, https://doi.org/10.1038/s41467-021-26401-w.

[37] S. Kumar, K. Karuppanan, G. Subramaniam, Omicron (BA.1) and sub-variants (BA.1.1, BA.2, and BA.3) of SARS-CoV-2 spike infectivity and pathogenicity: a comparative sequence and structural-based computational assessment, J. Med. Virol. 94 (2022) 4780–4791, https://doi.org/10.1002/jmv.27927.

[38] L. Wu, L. Zhou, M. Mo, T. Liu, C. Wu, C. Gong, K. Lu, L. Gong, W. Zhu, Z. Xu, SARS-CoV-2 Omicron RBD shows weaker binding affinity than the currently dominant Delta variant to human ACE2, Signal Transduct. Targeted Ther. 7 (2022), https://doi.org/10.1038/s41392-021-00863-2.

[39] O. Livnah, E.A. Bayer, M. Wilchek, J.L. Sussman, Three-dimensional structures of avidin and the avidin-biotin complex, Proc. Natl. Acad. Sci. USA 90 (1993) 5076–5080, https://doi.org/10.1073/pnas.90.11.5076.

[40] Z. Zhang, J. Zhang, J. Wang, Surface charge changes in spike RBD mutations of SARS-CoV-2 and its variant strains alter the virus evasiveness via HSPGs: a review and mechanistic hypothesis, Front. Public Health 10 (2022), https://doi.org/10.3389/fpubh.2022.952916.

[41] L. Mautner, M. Hoyos, A. Dangel, C. Berger, A. Ehrhardt, A. Baiker, Replication kinetics and infectivity of SARS-CoV-2 variants of concern in common cell culture models, Virol. J. 19 (2022) 76, https://doi.org/10.1186/s12985-022-01802-5.

[42] S. Cornélie, J. Hoebeke, A.-M. Schacht, B. Bertin, J. Vicogne, M. Capron, G. Riveau, Direct evidence that toll-like receptor 9 (TLR9) functionally binds plasmid DNA by specific cytosine-phosphate-guanine motif recognition, J. Biol. Chem. 279 (2004) 15124–15129, https://doi.org/10.1074/jbc.M313406200.

[43] X. Huang, E. Kon, X. Han, X. Zhang, N. Kong, M.J. Mitchell, D. Peer, W. Tao, Nanotechnology-based strategies against SARS-CoV-2 variants, Nat. Nanotechnol. 17 (2022) 1027–1037, https://doi.org/10.1038/s41565-022-01174-5.

[44] J. Zhu, Y. Su, Y. Tang, Disrupting ACE2 dimerization mitigates the infection by SARS-CoV-2 pseudovirus, Frontiers in Virology 2 (2022), https://doi.org/10.3389/fviro.2022.916700.

[45] Z. Ke, J. Oton, K. Qu, M. Cortese, V. Zila, L. McKeane, T. Nakane, J. Zivanov, C. J. Neufeldt, B. Cerikan, J.M. Lu, J. Peukes, X. Xiong, H.-G. Kräusslich, S.H. W. Scheres, R. Bartenschlager, J.A.G. Briggs, Structures and distributions of SARS-CoV-2 spike proteins on intact virions, Nature 588 (2020) 498–502, https://doi.org/10.1038/s41586-020-2665-2.